MDPI

Article

The Effect of Multiple Solder Reflows on the Formation of Cu_6Sn_5 Intermetallics and the Decomposition of SnAg3.0Cu0.5 Solder Joints in the Framework of Rework and Reuse of MLCC Components

Erik Wiss and Steffen Wiese *

Chair of Microintegration and Reliability, Faculty of Natural Sciences and Technology, Saarland University, 66123 Saarbrucken, Germany; erik.wiss@uni-saarland.de

* Correspondence: s.wiese@mx.uni-saarland.de; Tel.: +49-681-302-71820

Abstract: A rework of electronic assemblies and the reuse of electronic components are the most effective ways to reduce electronic waste. Since neither components nor substrates were developed with the intention of multiple usage, the question of how the integrity of lead-free solder joints is affected by multiple reflow operations is crucial for the implementation of any reuse strategy. Therefore, various types of 1206 multilayer ceramic capacitors (MLCCs) differing in their capacitance value and dielectric type (X5R, X7R, Y5V, NP0) were soldered on test printed circuit boards (PCBs) having a pure Cu-metallization surface in order to investigate the intermetallic reactions during multiple reflows. The metallization system on the MLCC-component side consisted of a thick film of Ni covered by galvanic-deposited Sn. The reflow experiments were conducted using a hypoeutectic SnAgCu solder. The results show the formation of a Cu_6Sn_5 intermetallic phase on both metallizations, which grows homogeneously with the number of reflows. Moreover, an ongoing decomposition of the solder into Ag-enriched and depleted zones was observed. The effect of these microstructural changes on the functionality of the solder joint was investigated by mechanical shear experiments and electrical four-point capacitance measurements.

Keywords: Cu_6Sn_5 intermetallic; intermetallic morphology; reflow; solder; SnAg3.0Cu0.5; multiple reflows; reuse; MLCC; shear test

Citation: Wiss, E.; Wiese, S. The Effect of Multiple Solder Reflows on the Formation of Cu_6Sn_5 Intermetallics and the Decomposition of SnAg3.0Cu0.5 Solder Joints in the Framework of Rework and Reuse of MLCC Components. *Metals* **2024**, *14*, 986. https://doi.org/10.3390/met14090986

Academic Editor: Chonghe Li

Received: 31 July 2024
Revised: 23 August 2024
Accepted: 25 August 2024
Published: 29 August 2024

Copyright: © 2024 by the authors. Licensee MDPI, Basel, Switzerland. This article is an open access article distributed under the terms and conditions of the Creative Commons Attribution (CC BY) license (https://creativecommons.org/licenses/by/4.0/).

1. Introduction

The increasing concern about the large number of end-of-life (EoL) electronics is discussed in different ways. While one group of authors focuses on the effective recovery of raw materials from electronic scrap [1–3] by different recycling methods, such as thermo-mechanical dismantling [4,5] or chemical disassembly [6], other authors consider the reuse of functioning components with significant remaining useful life (RUL) [7]. Desoldering processes, which are established for the rework of electronic assemblies such as printed circuit boards (PCBs), are mostly considered a technically feasible disassembly method for the reuse of components [8]. Some studies consider the effects of thermal [9,10] or mechanical loading [9,11] during the desoldering process. Since neither components nor substrates were developed with the intention of multiple usage, the question of how the integrity of lead-free solder joints is affected by multiple reflow operations is crucial for any reuse strategy.

Although the effects of multiple reflows on the microstructural and functional changes of solder interconnects are the subject of numerous publications, the reuse of component scenarios was not the subject of these studies. Nonetheless, the procedures and effects described in the existing literature guide the experimental program of the current study. The evolution of the shear strength and the electrical resistance of BGA solder balls after multiple reflows were investigated in [12,13], whereas the studies reported in [12–16] looked into interfacial reactions and their effect on the shear strength of solder bumps with

respect to the number of reflows as well as the effect of specific oxide additions (TiO_2) on intermetallic compound (IMC) growth on the Cu/solder interface [17]. Other studies focused on the shape and evolution of the Cu/solder-IMC morphology in Sn–x/Cu solder bumps after different numbers of reflow cycles [18–20], on the shape and thickness of solder/metallization-IMC in respect of different PCB surface finishes [21], and on the solder wettability and creep properties in dependence of the number of reflows [22].

Beside these predominately material science-centered studies, there are a smaller number of engineering-oriented investigations that are trying to examine the technology-related consequences of solder profile adjustments in multiple reflow operations in electronic manufacturing. Branzei and coworkers [23] worked on the optimization of reflow vapor phase soldering processes. The specimen consisted of a test PCB with surface-mounted device (SMD) 1206 zero-ohm resistors soldered to it. A similar specimen was used by Wirth and coworkers [24], who focused on the peak temperature and the time above liquidus in a traditional reflow process. In both studies, the shear strength and the IMC thickness were taken as parameters to evaluate the chosen reflow profile. The effects of soldering profiles on the functionality of multilayer ceramic capacitor (MLCC) components having X7R and Z5U dielectrics were the subject of studies by Jánó and coworkers published in [25,26]. While a significant effect of the soldering method and profile on the component parameters was shown, no further investigation into the mechanical and microstructural properties of the solder joints was undertaken.

In the framework of reuse of MLCCs by desoldering such components from an EoL-PCB and resoldering these components on a new PCB, ceramic capacitors are the more critical passive SMD components compared to resistors because the functionality of their ferroelectric body material may depend on acting external forces. Such forces may arise from residual stresses that are built up during de- and resoldering processes [10]. Therefore, the interfacial reactions of solder joints and their effect on the electrical and mechanical functionalities of MLCCs are of great interest for any reuse strategy. Thus, this study focuses on the specifics of the asymmetrical metallization system of soldered MLCCs with respect to the effects of multiple reflows. The investigated metallization system consists of pure copper on the side of the printed circuit boards (PCB), whereas on the MLCC-component side there is a thick film of Ni-metallization covered by a galvanic-deposited Sn layer. Also, the dependence of the MLCC's capacitance on the number of conducted reflow cycles is key to this investigation in order to evaluate the component functionality for the reuse case. A third important aspect deals with the solder joint's mechanical functionality for the given metallization system.

2. Materials and Methods

2.1. Sample Preparation

In order to investigate the effects of multiple solder reflow cycles on solder joints and passive SMD components, different samples were manufactured. For the first test, a PCB of size 160 mm × 100 mm was designed to hold eight MLCCs of size 1206 (length 3.2 mm and width 1.6 mm). Each pair of two soldering pads is connected to four additional pads to enable four-wire measurements of the capacitance of the MLCCs. The measurements have been carried out after every reflow cycle, up to a total of eight cycles. After machining the PCBs using a drilling machine, ProtoMat S103 (LPKF, Garbsen, Germany), the oxide layers of the PCB surface were removed with a rough pad to allow proper wetting of the solder paste. One piece of the manufactured test board is shown in Figure 1. The employed solder paste, a LOCTITE GC 10 SAC305T4 (Henkel, Düsseldorf, Germany) with a melting point of 217 °C, is a type 4 paste with a particle size distribution of 20 to 38 µm and a specified composition of 96.5 wt% Sn, 3.0 wt% Ag, and 0.5 wt% Cu, which is mixed homogeneously with a resin-based, halogen-free flux. The exact composition was not analyzed because the composition of the individual solder pad depots would vary in any case, given their relatively small volume. A compressed air dispenser, DX-250 (OKI, Cypress, CA, USA), was used for the deposition of the paste onto the solder pads. In the final step, the MLCC

components, which will be used for testing (samples), were placed with a manual pick-and-place system, ProtoPlace S (LPKF). The soldering process was made in an N_2 protective atmosphere using LPKF's batch reflow oven with the accompanying software FlowShow (version 2.10) to record the temperature profiles of the subsequent reflow processes.

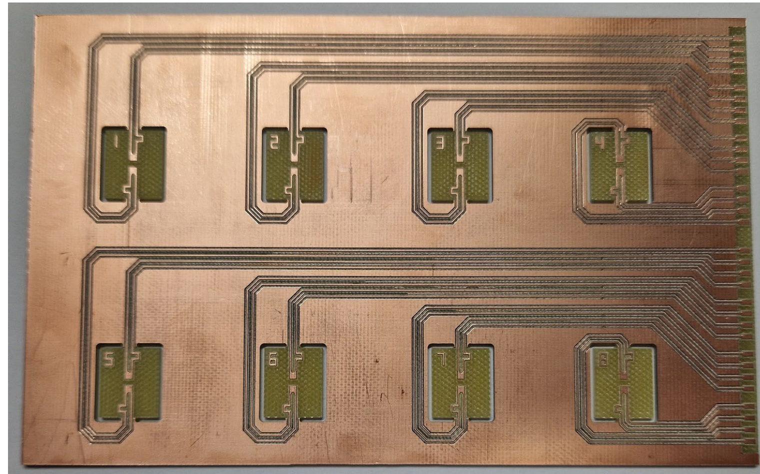

Figure 1. Layout of the electrical test-board (length 160 mm and width 100 mm) having a capacity to carry eight samples (C1–C8, solder pad layout for MLCC with 1206 size). Each pair of the MLCC soldering pads is connected to four pads on the right edge of the PCB to enable precise four-wire measurements of the MLCC's capacitances.

Table 1 shows the component types of MLCCs that were used for both the electrical measurements and the metallurgical analysis. Every type of component has the same size 1206, but they differ in their dielectric and thus in their properties, such as their operating temperature range and temperature-dependent change in capacitance. While the type X7R offers a large operating temperature range and an acceptable temperature coefficient, the type X5R can offer larger capacities. Type Y5V is very sensitive to temperature changes, which is why it is normally only used in circuits that can be operated at or near room temperature. Type NP0 is almost independent of the operating temperature, but it offers only low capacities at a high cost. Eight MLCCs of the same component type (C1–C8) were mounted on each test-board, resulting in a total of 32 samples (8 MLCC × 4 dielectric types). While the X5R and X7R MLCCs are from KEMET (Fort Lauderdale, FL, USA), the Y5V and NP0 are from Yageo (New Taipei City, Taiwan). For the metallurgical analysis, another test-board was used. It consists only of solder pads for the MLCCs, without additional pads to accommodate more MLCCs on one board. A total of four samples were used for the X7R component type.

Table 1. Summary of the different MLCC types that were used for the measurements.

Component Type	Dielectric	Nominal Capacitance	Maximum Temperature Coefficient	Number of Samples for Electrical Tests	Number of Samples for Metallurgical Analysis
KEMET C1206C106K4PAC7800+	X5R	10 µF ± 10%	±1071 ppm/K	8	0
KEMET C1206C474K5RACTU	X7R	470 nF ± 10%	±833 ppm/K	8	4
Yageo CC1206ZPY5V7BB475	Y5V	4.7 µF ± 20%	−7130 ... +1913 ppm/K	8	0
Yageo CC1206JRNPO9BN681	NP0	680 pF ± 5%	±30 ppm/K	8	0

In order to investigate the influence of multiple reflow cycles on the mechanical stability of the solder joints, a simple shear test was conducted. Therefore, small PCBs that can take up a single resistor were manufactured (see Figure 2). The resistors, model

RK73B2BTTD100J (KOA, Tokyo, Japan) with a resistance of 10 Ω, were soldered onto the pads in the same procedure as the MLCCs. Two additional pads allow in-situ monitoring of the health state of the solder joints. In each case, six samples were exposed to one, two, four, or eight reflow cycles (see Table 2).

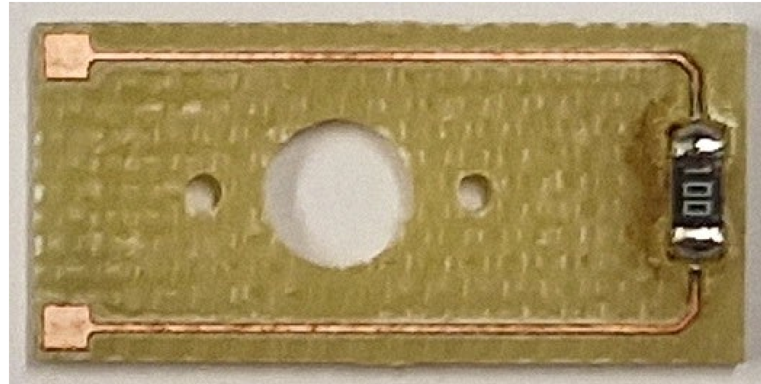

Figure 2. Layout of a test-PCB for the samples that were subjected to a shear test. The pads are connected to two additional pads on the left side of the PCB to allow in-situ monitoring of the solder joint health state during the mechanical test. The three holes in the middle are used to align and attach the samples to the holder of the testing machine.

Table 2. Summary of the resistors that were used for the shear test.

Component Type	Number of Reflow Cycles	Nominal Resistance	Temperature Coefficient	Number of Samples for Shear Tests and Metallurgical Analysis
KOA RK73B2BTTD100J	1	10 Ω ± 5%	±200 ppm/K	6
KOA RK73B2BTTD100J	2	10 Ω ± 5%	±200 ppm/K	6
KOA RK73B2BTTD100J	4	10 Ω ± 5%	±200 ppm/K	6
KOA RK73B2BTTD100J	8	10 Ω ± 5%	±200 ppm/K	6

2.2. Reflow Process

The samples were soldered in a batch reflow oven, ProtoFlow S (LPKF), into a nitrogen-protective atmosphere. Depending on the heat capacity of the components and substrates to be soldered, the reflow profile needs to be chosen in an appropriate manner to ensure that all solder joints melt during every reflow process. Therefore, the solder paste manufacturer gives various recommendations that differ in the preheat time, the heating rate, the peak time, and the peak temperature. First attempts showed that good results could be achieved using a preheat phase of 160 °C for 70 s to heat up the components uniformly and activate the flux, and a peak phase of 250 °C for 80 s. While the heating rate of approximately 0.95 °C/s could not be changed, the cooling rate was set to approximately 1.56 °C/s. Note that the temperatures are the air temperature and not the substrate temperature. The time-temperature curve of the reflow profile is shown in an idealized form without noise in Figure 3.

In the case of the MLCC samples, the capacitance values were measured after every reflow cycle. After every reflow, a sufficiently long cooling time was chosen to bring the samples securely to room temperature in order to minimize the potential temperature error for the capacitance measurement on MLCCs. In the case of the resistor samples for mechanical functionality, the respective shear test was started when the stated number of reflow cycles (see Table 2) had been carried out.

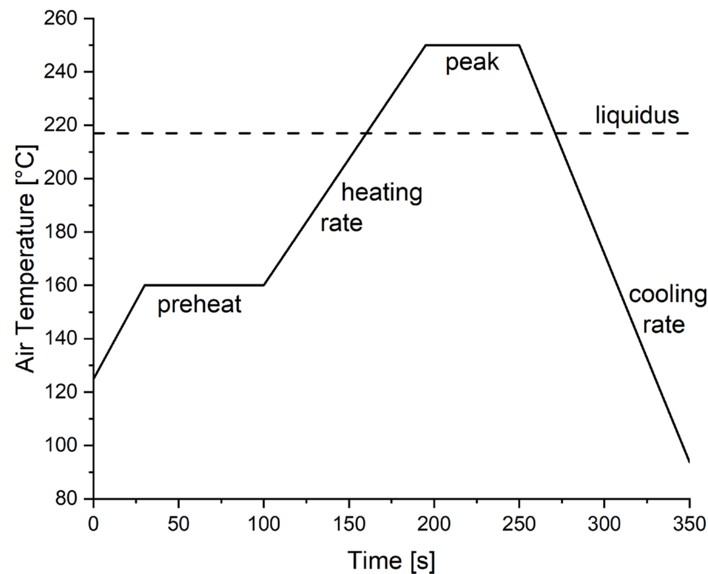

Figure 3. Time-temperature curve of the reflow profile that was used for the experiments. The graph summarizes the recordings of the subsequent reflow process in a typical and idealized form (without noise). Every reflow process had an identical profile. The reflow soldering has been carried out in a batch reflow oven, ProtoFlow S (LPKF), using a nitrogen-protective atmosphere.

2.3. MLCC Measurements

The MLCC measurements were realized using an LCR meter E4980AL (Keysight, Santa Rosa, CA, USA) and a specially developed measurement adapter (see Figure 4). The measurement device is connected to this adapter using four BNC connectors, which are adapted to four pin heads. Its grid exactly matches one of the Cu pads on the MLCC board, allowing easy measurement of the capacitance and resistance values. After the pin heads have contact with the Cu pads, the measurement is initiated by a manual trigger on the device.

Figure 4. Specially developed measurement adapter that is connected to the measurement device via four BNC connectors, which bring the shielded measurement connections to the adapter. These measurement connections are redistributed by the PCB to four pin heads, whose grid exactly matches one of the Cu pads. After the pin heads have been brought into contact with the pads, the measurement is initiated (manual trigger).

The capacitance of the used MLCCs is less than or equal to 10 µF, which is why the parallel measurement mode with a voltage of 1 V was chosen. In this mode, the series

resistance R_s and the series inductance L_s, which are mainly derived from the resistance of the measurement wires and the capacitor plates, are ignored. Only the parallel resistance R_p, mainly caused by polarization losses, and the capacitance are measured. The equivalent circuit diagram of a real capacitor is shown in Figure 5.

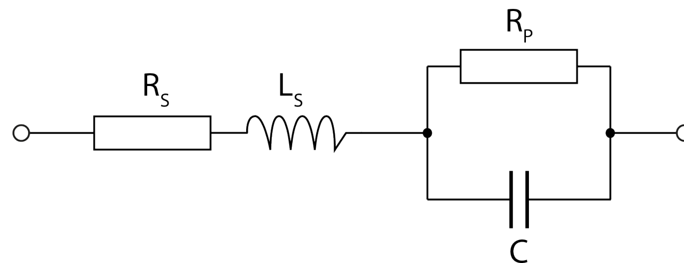

Figure 5. Equivalent circuit diagram of a real capacitor, consisting of a series resistance R_s, a series inductance L_s, a parallel resistance R_p, and the capacitance C, adapted from [27].

In accordance with the international standard norm IEC 60384-1 [28], a frequency of 1 kHz was chosen for the X5R, X7R, and Y5V MLCCs (1 nF $\leq$ C $\leq$ 10 µF), while a frequency of 300 kHz instead of 1 MHz had to be used for the NP0 MLCCs (C $\leq$ 1 nF) due to the limitations of the measurement device. An overview of the measurement settings is shown in Table 3. The measurements, which were conducted after every reflow cycle, were averaged over five net power line cycles (NPLCs) to minimize interfering noises and thus stabilize the results. After five reflow cycles, the measurements had to be paused until the next day.

Table 3. Summary of the measurement settings that were used for the different MLCCs.

Model	Dielectric	Nominal Capacitance	Measurement Voltage	Measurement Frequency	NPLC
KEMET C1206C106K4PAC7800+	X5R	10 µF ± 10%	1 V	1 kHz	5
KEMET C1206C474K5RACTU	X7R	470 nF ± 10%	1 V	1 kHz	5
Yageo CC1206ZPY5V7BB475	Y5V	4.7 µF ± 20%	1 V	1 kHz	5
Yageo CC1206JRNPO9BN681	NP0	680 pF ± 5%	1 V	300 kHz	5

2.4. Mechanical Test Setup

The shear tests were conducted on a slightly modified mechanical test setup that was developed to conduct mechanical tests on packaging materials (specialized samples), i.e., tensile tests on PCB Cu-trace sheet material [29], or electronic components, i.e., cyclic bending experiments on QFN samples that were soldered on a PCB [30]. The setup is built around a stereo zoom microscope, SteREO Discovery.V20 (Zeiss, Oberkochen, Germany), with two attached cameras to allow the possibility of image acquisition during the mechanical experiments for further evaluation using digital image correlation (DIC) methods, which is important to analyze complex deformation states as in the case of the bending of the soldered QFN samples [30]. In this study, no use of the DIC method was made because, in order to evaluate the bonding strength as a parameter of mechanical functionality, no deformation information was needed. The shear test conducted on the MLCC components refers only to the fracture strength of the weaker of the two solder joints. The setup is shown in Figure 6.

A threaded rod is mounted on a motor-driven linear table (A), which can provide a load of up to 200 N. At the other end, a shear chisel made of a small piece of PCB material with a removed Cu layer is attached to a holder, transferring the load of the actuator to the sample (see Figure 7). This special, non-conductive chisel was chosen because a metal one would possibly short-circuit the Cu pads to which the resistor was soldered and thus prevent correct crack detection within the solder joints. On the opposite side, the prepared

sample is clamped under the microscope (D) in another sample holder, which is attached to a three-dimensional force sensor (B) K3R110 (ME-Meßsysteme, Hennigsdorf, Germany) in order to record not only the force in the shear direction but also any torques. The sensor is connected via amplifiers (C) GSV-2TSD-DI (ME-Meßsysteme) to a multifunction I/O device PCIe-6341 (National Instruments, Austin, TX, USA). The crack detection circuit (E) monitors the output voltage of an operational amplifier in whose positive input path the pads of the resistor samples are inserted. A crack in one of the solder joints results in a change in the measured voltage and thus indicates a failure. The setup is controlled by LabVIEW (National Instruments).

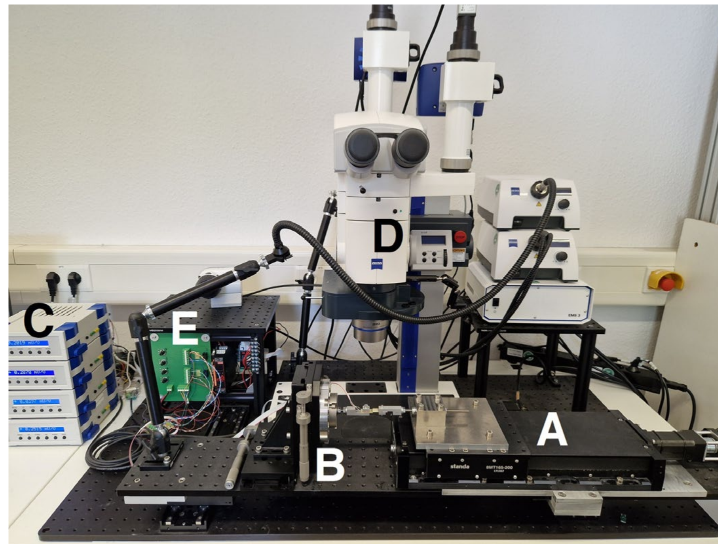

Figure 6. Overview of the mechanical test setup presented in [29,30]. The main components of the setup are labeled as follows: A: Actuator. B: Three-axis force sensor. C: Measurement amplifiers (for force sensors). D: Stereo zoom microscope with illumination units. E: Crack detection circuit.

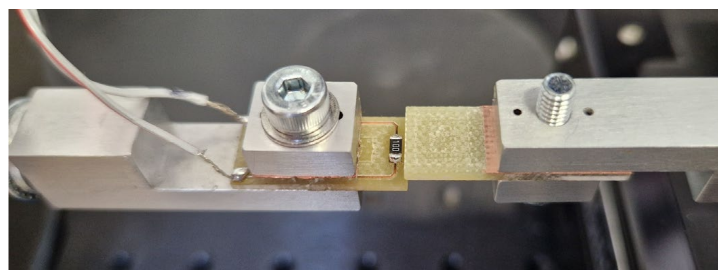

Figure 7. Detailed view of the experimental setup. The displacement of the actuator and thus a force are transferred to the resistor via a small PCB, which is electrically isolated to not influence the electrical measurement. A crack formation within one of the solder joints results in an interruption of the electrical pathway between the two wires on the left side, which are connected to the crack detection circuit.

All shear tests have been conducted with a cross-head speed of 0.1 mm/s, which corresponds to the international standard norm IEC 62137-1-2 [31]. Although the estimated shear rate of 1/s is relatively high, similar cross-head speeds were chosen by other studies, i.e., 0.1 mm/s [14], 0.2 mm/s [12,15], 0.3 mm/s [24], and 0.5 mm/s [26]. These shear rates do not represent the usual thermal cyclic loading appropriately. In that respect, the practice of conducting shear tests seems to be a bit controversial. Obviously, under these conditions, the standard shear test is unable to determine the comprehensive mechanical behavior or the long-term reliability of solder joints. The determination of these properties requires creep tests and thermal cycle tests. However, such experiments take a very long time

to be carried out. Moreover, creep experiments cannot be conducted on the presented specimens because the stiffness of the PCB base material is very time-dependent. The high shear rate of the standard shear test helps to suppress the viscoelastic PCB base material behavior influence on the shear strength results, except for shock resistance testing. The latter requires much higher shear rates in the range of 100–2000 mm/s, as used in [32].

In this study, the shear tests were conducted after one, two, four, and eight reflow cycles, with a total of six samples per condition ($6 \times 4 = 24$ samples).

2.5. SEM and EDX Analysis

To allow scanning electron microscopy (SEM) and energy dispersive X-ray spectroscopy (EDX) analysis, the samples had to be prepared in a specific way using several preparation steps. First step: the diced samples were embedded in epoxy using the EpoFix kit (Struers, Ballerup, Denmark) and cut with an ISOMET 4000 precision saw (Buehler, Lake Bluff, IL, USA). Second step: after hardening, the samples were ground on SiC foils with different grits of 500 and 1200 on a LabPol-25 (Struers). Third step: polishing using various diamond suspensions having 9 µm, 3 µm, and 1 µm particle sizes on a Tegramin-25 (Struers). Fourth step: final polishing with a colloidal silicon oxide on a Saphir Vibro (ATM Qness, Mammelzen, Germany) vibratory polishing machine, resulting in an extremely even surface with ultra-low roughness. Fifth step: the prepared samples were coated with a very thin carbon film using a Q150T Coater (Quantum Design, Pfungstadt, Germany) to avoid charging effects during the SEM operation and to not disturb the EDX analysis. The target thickness of the carbon film was 20 nm to retain the even surface of the samples. The SEM and EDX analyses were realized using an EVO MA15 (Zeiss) with an LaB_6 cathode, an accelerating voltage of 20 kV and a beam current of 40 µA, and an XFlash detector (Bruker, Billerica, MA, USA) with an energy resolution of 123 eV. The images were taken in secondary electrons (SE) mode. In the case of the MLCCs, the analysis has been carried out at almost the same location between the MLCC termination and the Cu pad underneath (see Figure 8). For a more accurate analysis, line scans that start at the termination of the MLCC component and end at the Cu pad were performed (see Figure 9). In the case of the resistors that were subjected to the shear test, one side of the ragged component was analyzed. Additionally, a more detailed picture of the location above the Cu pad was analyzed.

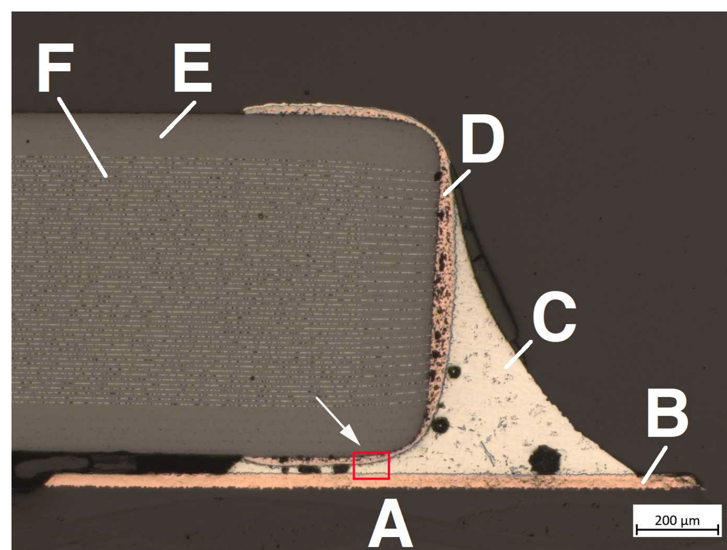

Figure 8. Light microscopy image of an X7R MLCC (Magnification: 5×). The red box between the MLCC and the Cu pad marks the location of the SEM and EDX analysis. A: PCB base material. B: Cu pad of the PCB. C: Solder joint. D: Cu metallization and Ni termination. E: MLCC ceramic body. F: Inner electrodes.

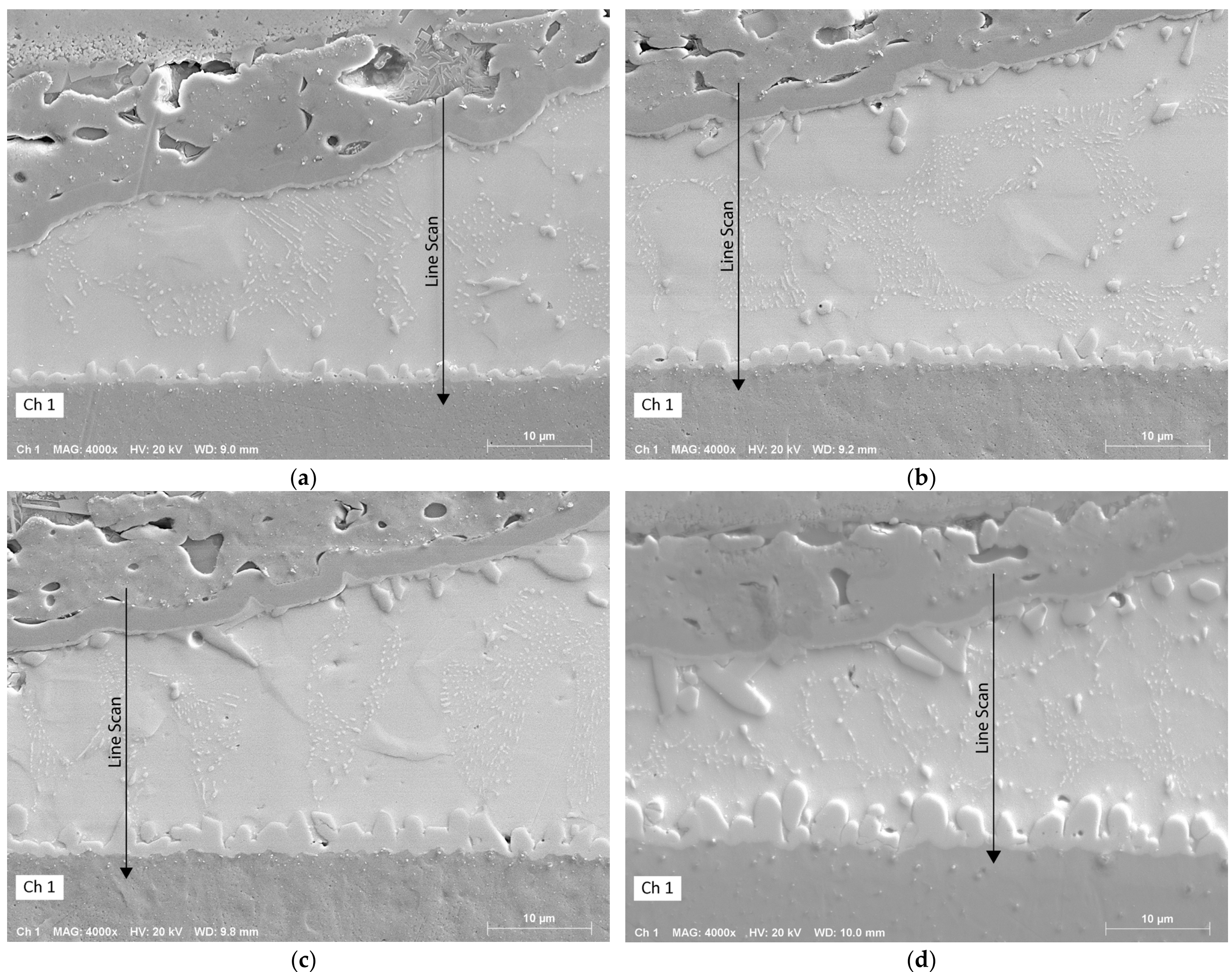

Figure 9. SEM images in SE mode with an enlarged view of the red box area of Figure 8. Path along which the line scans were performed after the (**a**) first, (**b**) second, (**c**) fourth, and (**d**) eighth reflow cycles, starting within the Ni-thick film layer (termination) of the MLCC and ending in the Cu metallization of the PCB.

3. Results

3.1. IMC Formation

The IMC formation at the solder/Cu interface was analyzed by EDX. Although only diffraction methods are able to unambiguously identify IMCs by their crystal properties, the tight framework of reflow experiments in a clearly defined temperature range makes the EDX analysis a more suitable and convenient tool, given its unexpensive sample preparation and thus higher throughput to achieve more statistical confidence in the overall picture. Figures 10–13 show a detail of the solder meniscus (see Figure 8) as SEM photographs in SE mode and as an EDX map. The composite map, which contains counts for the elements Ni, Cu, Ag, and Sn, is also displayed for the individual elements in order to more clearly show where the four elements intermix with each other and where the elements are separated from each other. Additionally, Figure 14 shows the composition of the four elements and the separated Ag concentration along a path, starting from the MLCC termination and ending in the Cu metallization of the PCB (see Figure 9).

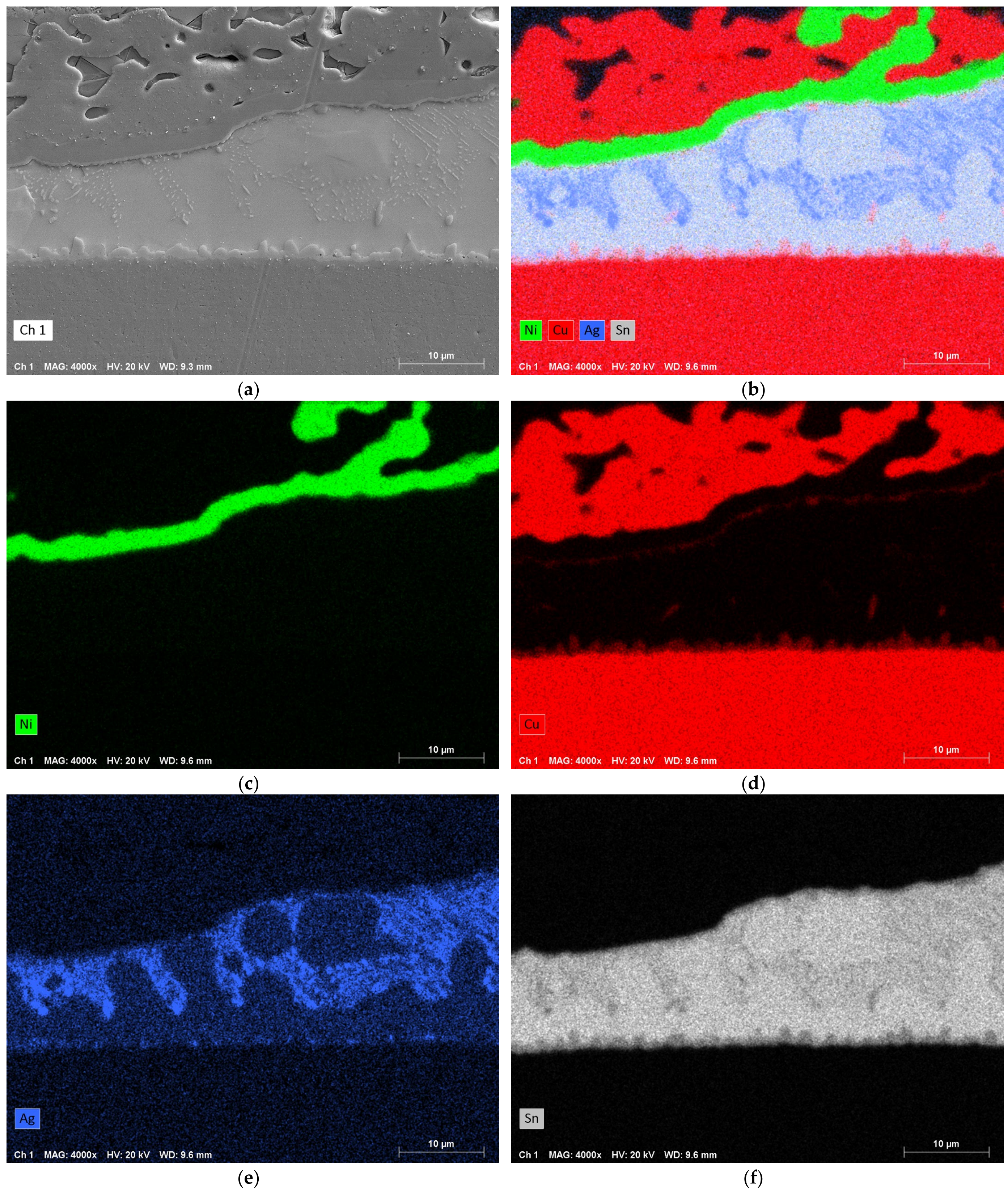

Figure 10. EDX analysis of an X7R MLCC after the first reflow cycle with a magnification of 4000×. (**a**) SEM image in SE mode. (**b**) Combined EDX maps of Ni, Cu, Ag, and Sn. (**c**) EDX map of Ni. (**d**) EDX map of Cu. (**e**) EDX map of Ag. (**f**) EDX map of Sn.

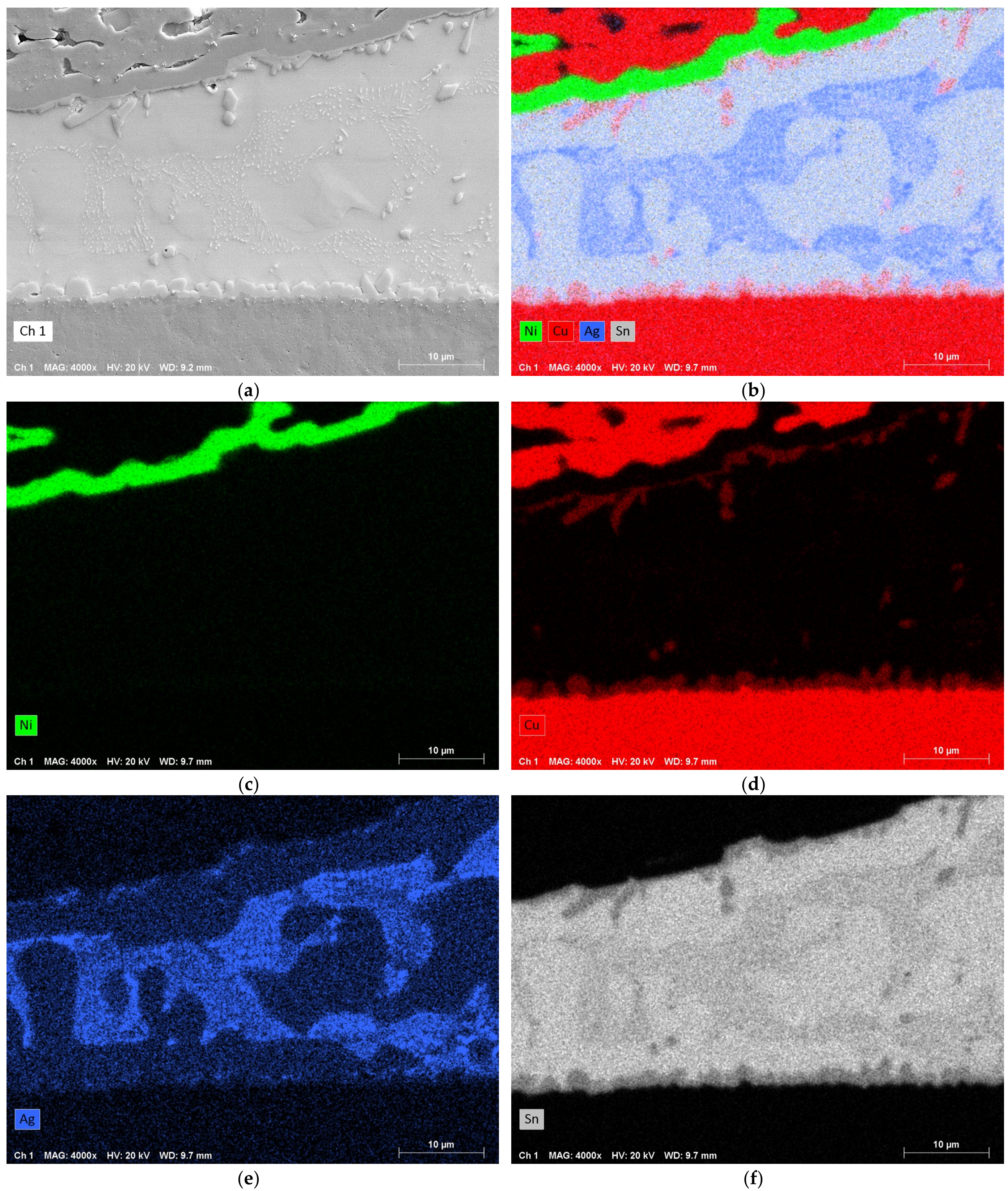

Figure 11. EDX analysis of an X7R MLCC after the second reflow cycle with a magnification of 4000×. (**a**) SEM image in SE mode. (**b**) Combined EDX maps of Ni, Cu, Ag, and Sn. (**c**) EDX map of Ni. (**d**) EDX map of Cu. (**e**) EDX map of Ag. (**f**) EDX map of Sn.

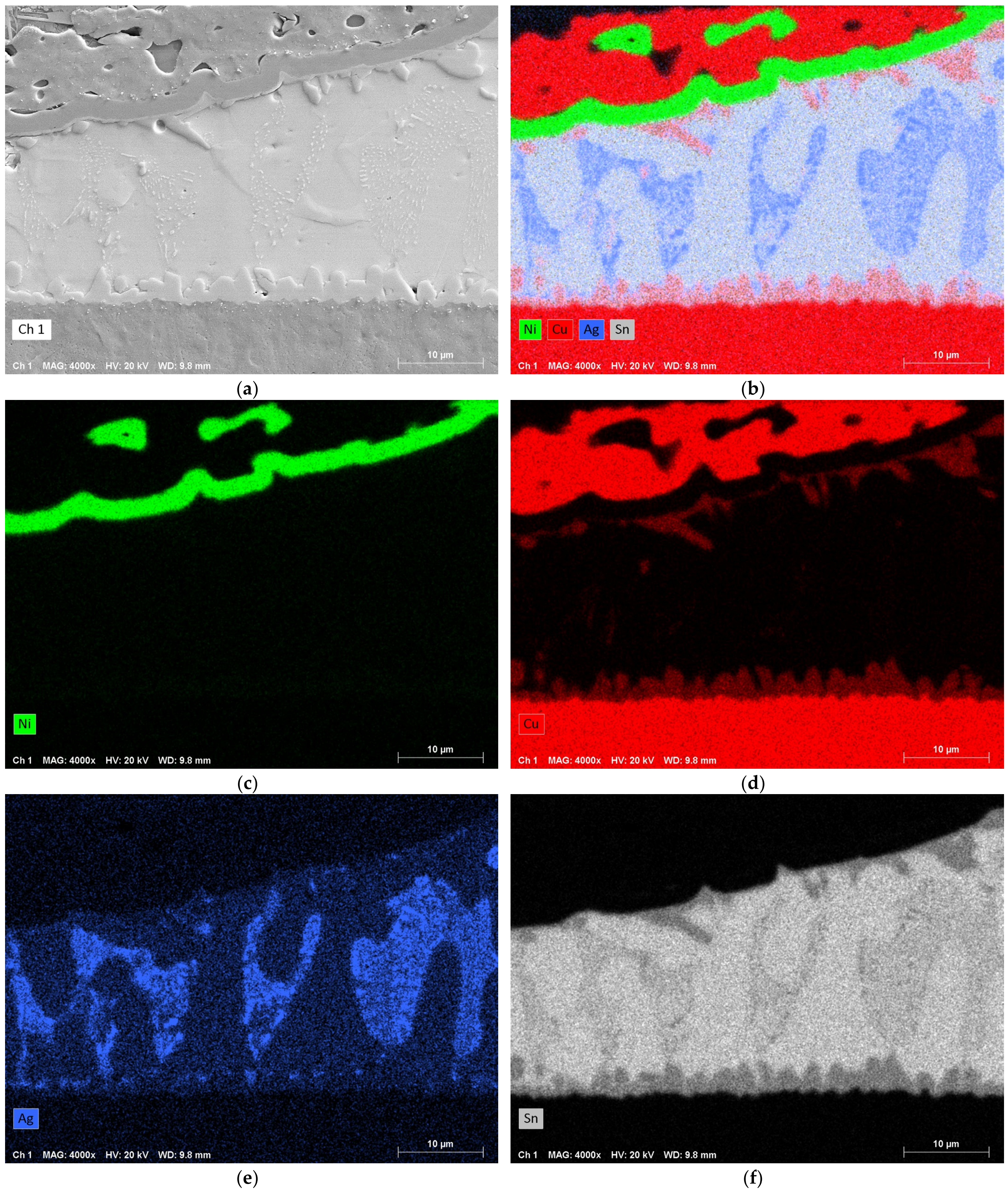

Figure 12. EDX analysis of an X7R MLCC after the fourth reflow cycle with a magnification of 4000×. (**a**) SEM image in SE mode. (**b**) Combined EDX maps of Ni, Cu, Ag, and Sn. (**c**) EDX map of Ni. (**d**) EDX map of Cu. (**e**) EDX map of Ag. (**f**) EDX map of Sn.

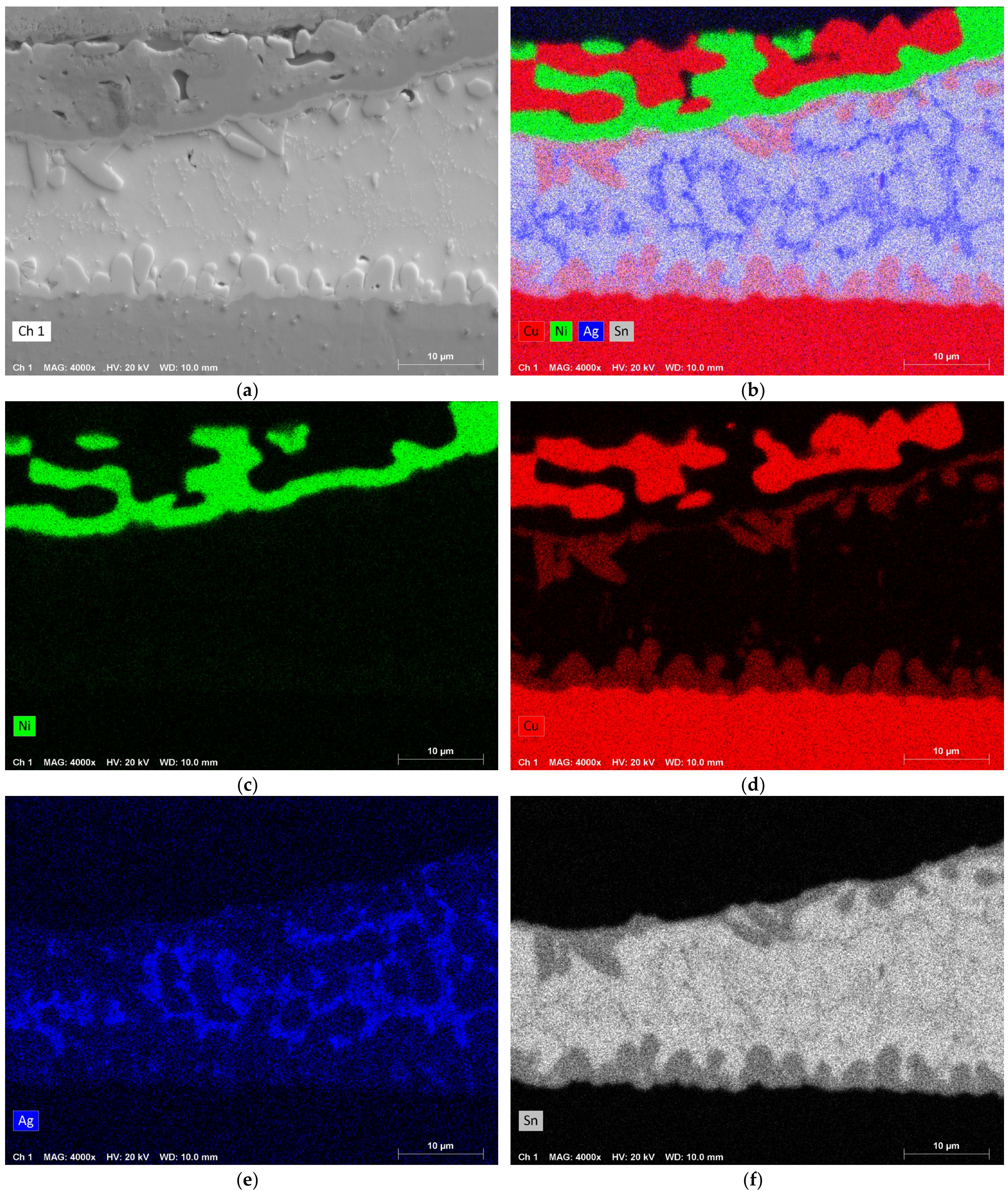

Figure 13. EDX analysis of an X7R MLCC after the eighth reflow cycle with a magnification of 4000×. (**a**) SEM image in SE mode. (**b**) Combined EDX maps of Ni, Cu, Ag, and Sn. (**c**) EDX map of Ni. (**d**) EDX map of Cu. (**e**) EDX map of Ag. (**f**) EDX map of Sn.

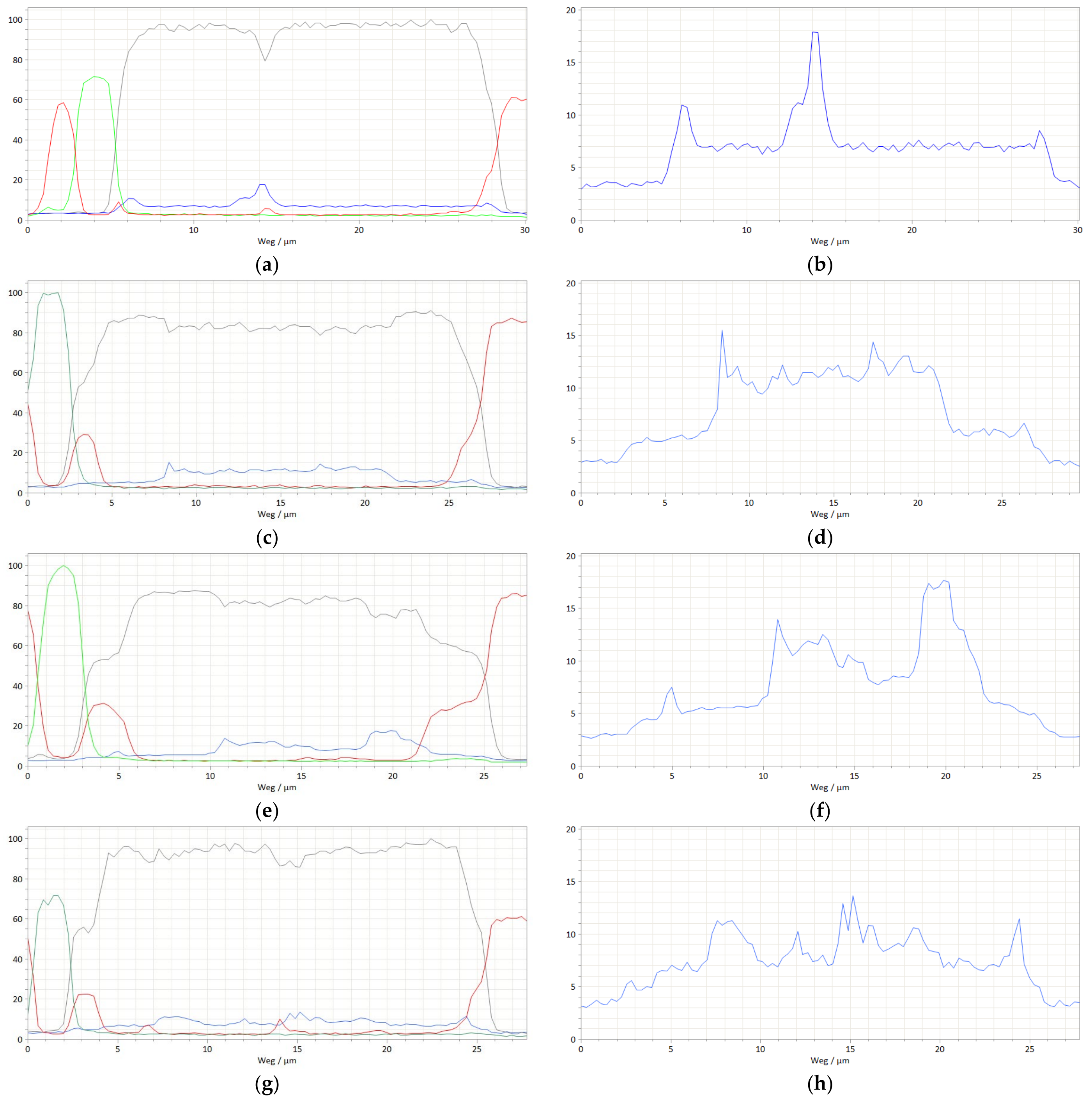

Figure 14. Line scan overviews along the given path (compare Figure 9) of an X7R MLCC after the (**a**,**b**) first, (**c**,**d**) second, (**e**,**f**) fourth, and (**g**,**h**) eighth reflow cycle, showing the evolution of the Cu_6Sn_5 IMC (left-hand side) and the distribution of Ag within the solder (right-hand side), standardized to a total concentration of 100% (*y*-axis). Green: Ni. Red: Cu. Gray: Sn. Blue: Ag. While a continuous IMC layer has already formed at the interface solder/PCB metallization after the first reflow cycle, it takes four reflow cycles to form a proper IMC layer at the interface solder/component termination. During several reflow cycles, the Ag depletion zones at the interfaces diminish, and the Ag seems to distribute more and more uniformly within the solder paste. The depicted diagrams were taken directly from the EDX software QUANTAX ESPRIT (version 2.0) without editing. The ordinate shows the concentration in %, and the abscise ('Weg/µm') shows the distance along the scanning path. The algorithm of the used EDX software seems not always to be able to standardize the total concentration to 100%, which causes the differences in the tin concentration in the center of the solder joints.

Figure 10 shows the IMC formation after the first reflow (=solder paste is melted and reacts for the first time with the PCB- and component metallization). While the interface solder/PCB-metallization shows a tightly packed Cu_6Sn_5 IMC layer formation with a thickness of a few micrometers, there has only been a sparse growth of small individual Cu_6Sn_5 IMC cells at the interface solder/component metallization.

After the second reflow (the solder joint is remelted and reacts with the IMC on both interfaces, solder/PCB and solder/component metallization), a significant growth of the Cu_6Sn_5 IMC at the interface solder/component metallization can be observed (Figure 11). Although this compound is still not a coherent layer on top of the Ni diffusion barrier of the component, its appearance is much more pronounced than after the first reflow. This effect of the subsequent formation of Cu_6Sn_5 IMC (on the solder/PCB side after the first reflow and on the solder/component side after the second reflow) can be very well recognized from the results of the EDX line scans depicted in Figure 14. While there is a notable overlap area where the Sn-line and the Cu-line cross each other on the right-hand side of Figure 14a (at 28 μm), there is only a small Cu-line peak on the left-hand side (at 5.5 μm). In contrast, Figure 14c shows two distinct overlap areas for the Sn-line and Cu-line on the left-hand side (at 3.5 μm) and on the right-hand side (at 26.5 μm). The same picture is shown in the diagrams in Figure 14e,g, which depict the line scans for the sample after four and eight reflow cycles.

If the microstructure of the solder joint is compared between the first and second reflows, a large contrast in the distribution of Ag can be observed. While after the first reflow, an Ag depletion zone can only be observed on top of the Cu_6Sn_5 IMC at the interface solder/PCB metallization (Figure 10), this Ag depletion zone can be observed on both interfaces (solder/PCB and solder/component metallization) after the second reflow (Figure 11). The Ag-depleted zone diminishes with the number of reflows, and the Ag distribution becomes more and more equal (Figure 14b,d,f,h), as the pure beta-tin areas and the mixed Ag_3Sn/Sn areas continuously shrink (Figures 12 and 13). This effect of the subsequent decomposition of the SnAg3.0Cu0.5 solder is also indicated by the results of the EDX line scans depicted in Figure 14. The enlarged Ag-line scan after the first reflow (Figure 14b) shows two peaks (at 6 μm and 14 μm), which are closer to the component side. Particularly, the peak at 6 μm is directly on the solder/component interface. In contrast, the Ag-line scan after the second reflow (Figure 14d) shows a pronounced plateau (from 8 μm to 22 μm), which is away from either interface (to the PCB or the component). The Ag-line scan after the fourth reflow (Figure 14f) shows peaks at both interfaces (at 5 μm and 20 μm) as well as a central peak (from 10 μm to 16 μm), while the Ag-line scan after the eighth reflow (Figure 14h) shows a plateau reaching from one interface to the other one (from 5 μm to 24 μm).

After four reflow cycles, a Cu_6Sn_5 IMC layer has formed that covers the Ni diffusion barrier of the component nearly entirely (Figure 12). The further growth of this Cu_6Sn_5 IMC on the component side is different from that on the PCB side. While the PCB side Cu_6Sn_5 IMC has a spherical morphology in accordance with the fundamental growth kinetics reported in [19], the further growth of the component side Cu_6Sn_5 IMC occurs in single locations with a rather dendritic morphology (Figure 13). Therefore, it is very difficult to determine the IMC thickness at the solder/component metallization interface. The results of the IMC thickness characterization are displayed in the diagrams in Figure 15. It was observed that the initial thickness of the Cu_6Sn_5 IMC that grows on the Cu metallization of the PCB is approximately 2 μm, while the continuous layer of the Cu_6Sn_5 IMC on the Ni metallization on the component side never exceeds 1 μm. However, the average Cu_6Sn_5 IMC layer thickness is similar on both sides, beginning with the second reflow. The EDX line scans depicted in Figure 14 indicate that the Cu_6Sn_5 IMC on both interfaces is widening during the first couple of reflows. As the Cu-line peaks in Figure 14g show, the Cu_6Sn_5 IMCs seem to be present not only on the interfaces but also in the center of the solder joint after a larger number of reflows. The presence of Cu_6Sn_5 IMC particles within the solder material can also be concluded from the EDX mapping depicted in Figure 13.

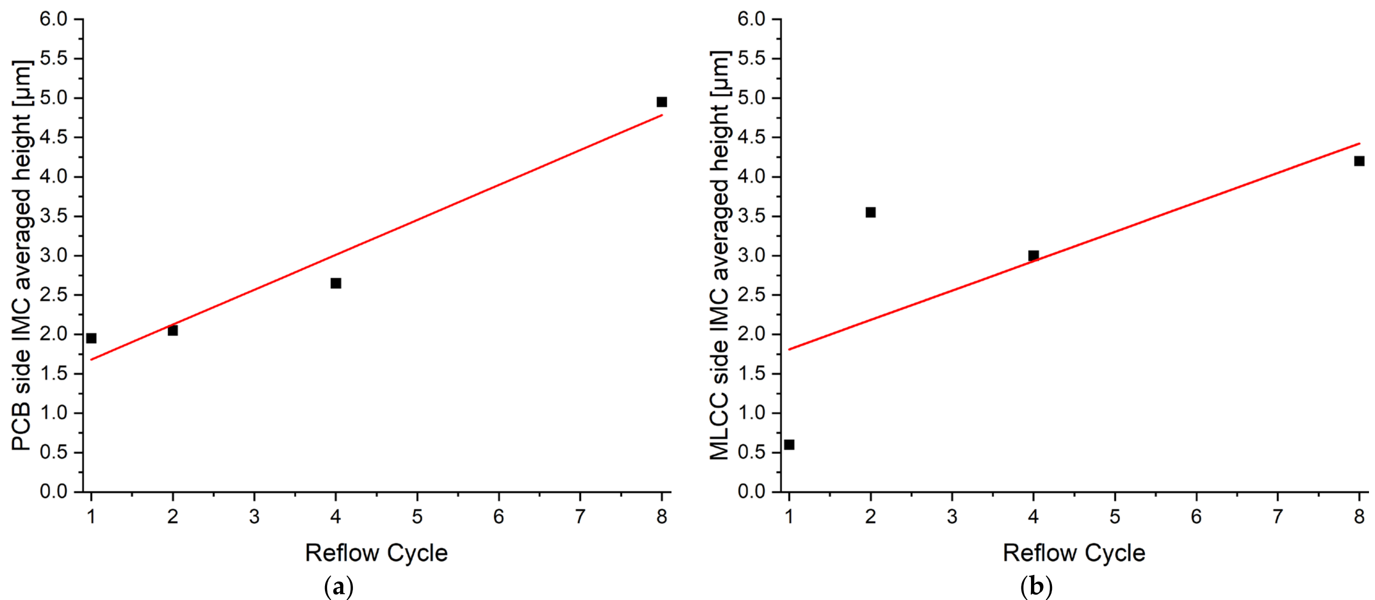

Figure 15. Averaged height of the Cu6Sn5 IMC at the interface between (**a**) the solder paste and the PCB metallization (R^2 = 0.96), and (**b**) the solder paste and the MLCC component (R^2 = 0.54). As the values were only measured after one, two, four, and eight reflow cycles, the remaining values were interpolated using a linear fit.

The formation of the Ni-layer in the EDX-mappings of Figures 10b, 11b, 12b and 13b appears to be irregular because parts of the Ni layer are situated underneath the Cu-layer of the MLCC. The most extreme case is shown in Figure 13b, where the Ni layer can be found directly on the interface to the $BaTiO_3$ body. It seems that the viscous Ni thick film paste (which shows no porosity) was optimized to fill in all the pores of the Cu thick film paste, which was supposedly optimized for other properties, i.e., adhesion to the $BaTiO_3$ body. What can be observed from all EDX-mappings is that the dipping process for the fabrication of MLCC terminals produces a closed Ni-layer on top of the Cu-layer and thus protects the Cu-layer from any reaction with the liquid Sn during soldering.

3.2. Capacitance Measurements

The samples of the KEMET C1206C106K4PAC7800+ (dielectric X5R, size 1206, nominal capacitance 10 µF ± 10%) were measured in parallel mode over 5 NPLCs using a voltage of 1 V and a frequency of 1 kHz. The Cycle-Capacitance diagram of eight samples (C8 for four reflow cycles and C1-C7 for eight reflow cycles) is shown in Figure 16.

As can be seen from the diagram, all X5R MLCCs show similar changes in their electrical functionality during multiple reflow cycles. No matter how many reflow cycles were conducted, all the measured values remain within the capacitance range specified by the manufacturer (9–11 µF). The biggest increase in the capacitance between two reflow cycles occurs after the second one (3–5.5%), with further changes between −2.5% and 3.5%. The reason for the large increase in capacitance between the first two reflow cycles remains unclear, but the solder joint may be one possible reason. After the sixth reflow cycle, the values remain quasi-constant, with small changes between −0.5% and 0.5%. Referring back to the initial value, the largest average change was reached after the eighth reflow cycle (averaged 5.2%), but it is only a slight increase when compared to the second one (averaged 4.6%). It can be assumed that the small, minimal turning point after the fifth reflow cycle is caused by the interruption of measurements due to any relaxation processes within the materials.

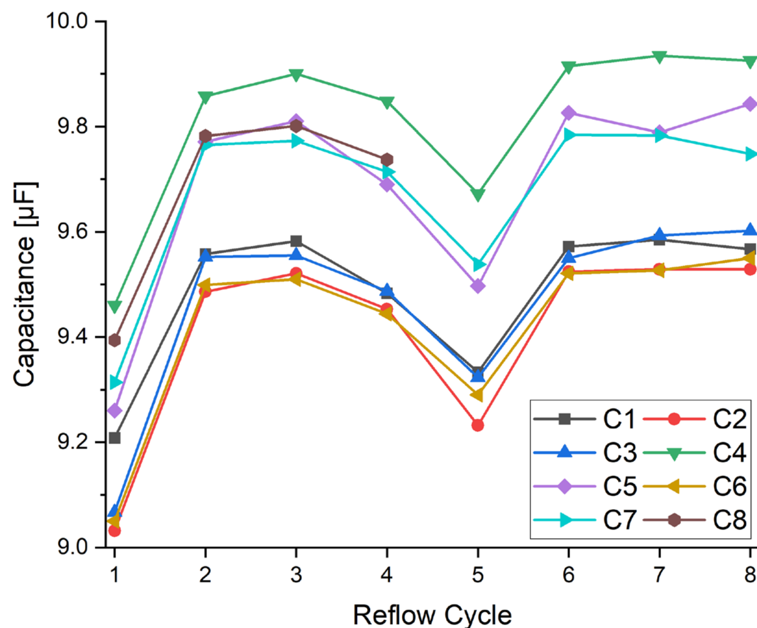

Figure 16. Cycle-Capacitance diagram of the measured values of KEMET C1206C106K4PAC7800+ (dielectric X5R, size 1206, nominal capacitance 10 µF ± 10%) for eight reflow cycles. The values behave in a similar way, including an increase after the first two reflow cycles, a decrease between the third and the fifth one, and further increases during the last three ones.

The samples of the KEMET C1206C474K5RACTU (dielectric X7R, size 1206, nominal capacitance 470 nF ± 10%) were measured in parallel mode over 5 NPLCs using a voltage of 1 V and a frequency of 1 kHz. The Cycle-Capacitance diagram of eight samples (C8 for four reflow cycles and C1–C7 for eight reflow cycles) is shown in Figure 17.

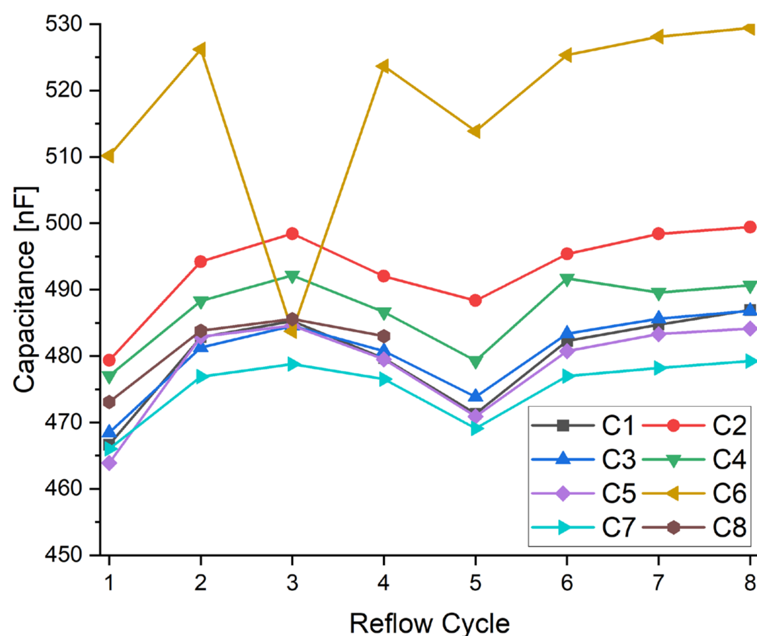

Figure 17. Cycle-Capacitance diagram of the measured values of KEMET C1206C474K5RACTU (dielectric X7R, size 1206, nominal capacitance 470 nF ± 10%) for eight reflow cycles. Except for sample number 6, the values behave in a similar way, including an increase after the first two reflow cycles, a decrease between the third and the fifth one, and further increases during the last three ones.

With the exception of C6, whose capacitance value is already outside the capacitance range specified by the manufacturer (423–517 nF) after two reflow cycles, the other samples remain within the range. As in the case of the X5R MLCCs, the X7R MLCCs show similar changes, with the biggest increase after the second reflow cycle (2.2–4.2%), with further changes between −1.8% and 2.6%. As before, the values remain quasi-constant after the sixth reflow cycle (−0.6% and 0.8%), with a maximum variation after the eighth reflow cycle (averaged 3.8% compared to 2.9% after the second one).

The samples of the Yageo CC1206ZPY5V7BB475 (dielectric Y5V, size 1206, nominal capacitance 4.7 µF ± 20%) were measured in parallel mode over 5 NPLCs using a voltage of 1 V and a frequency of 1 kHz. The Cycle-Capacitance diagram of eight samples (C8 for four reflow cycles and C1-C7 for eight reflow cycles) is shown in Figure 18.

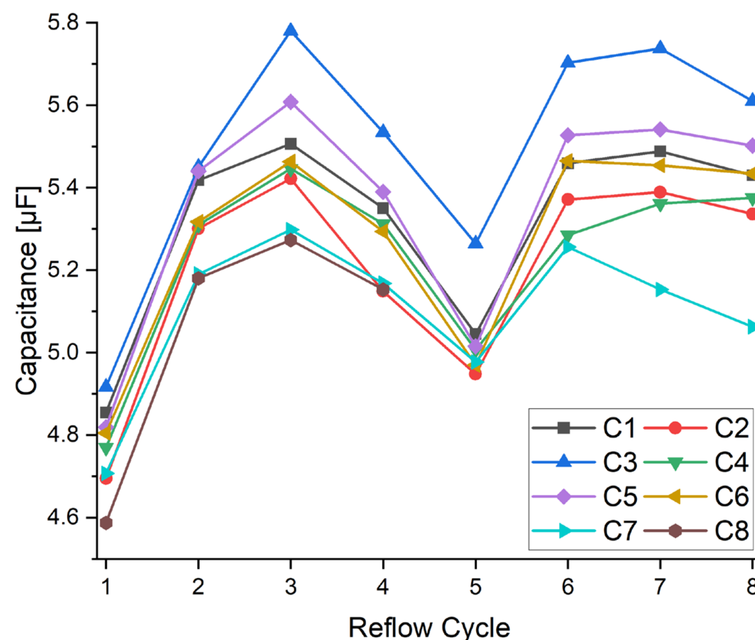

Figure 18. Cycle-Capacitance diagram of the measured values of Yageo CC1206ZPY5V7BB475 (dielectric Y5V, size 1206, nominal capacitance 4.7 µF ± 20%) for eight reflow cycles. The values behave in a similar way, including an increase after the first two reflow cycles, a decrease between the third and the fifth one, and further increases during the last three ones.

With the exception of C3, whose capacitance value is already outside the capacitance range specified by the manufacturer (3.76–5.64 µF) after three reflow cycles, the other samples remain within the range, albeit at the upper limit. The basic shape of the changes in capacitance of the Y5V MLCCs is similar to the first two types, but the relative changes are much greater. After the second reflow cycle, the values increase by 9.5% to 13%, with further changes between −7% and 10%. Again, the values remain comparatively constant, with small changes between −2% and 1.5% after the sixth reflow cycle. The largest averaged change is reached after the third reflow cycle with 14.8%, while it is only 12.4% after the eighth reflow cycle.

The samples of the Yageo CC1206JRNPO9BN681 (dielectric NP0, size 1206, nominal capacitance 680 pf ± 5%) were measured in parallel mode over 5 NPLCs using a voltage of 1 V and a frequency of 300 kHz. The Cycle-Capacitance diagram of eight samples (C8 for four reflow cycles and C1–C7 for eight reflow cycles) is shown in Figure 19.

Without exception, the measured values of the NP0 MLCCs remain almost constant and thus in the specified capacitance range specified by the manufacturer (646, 714 pF). They exhibit the highest robustness against the temperature effects of the soldering processes. The change in capacitance values between two reflow cycles and the changes referenced to the initial value vary in a range between −0.2% and 0.2%. Table 4 summarizes the

results of all the capacitance measurements. While the changes in the X5R and X7R types are mid-range, the Y5V experiences the highest changes. At NP0, nearly no change in capacitance could be observed.

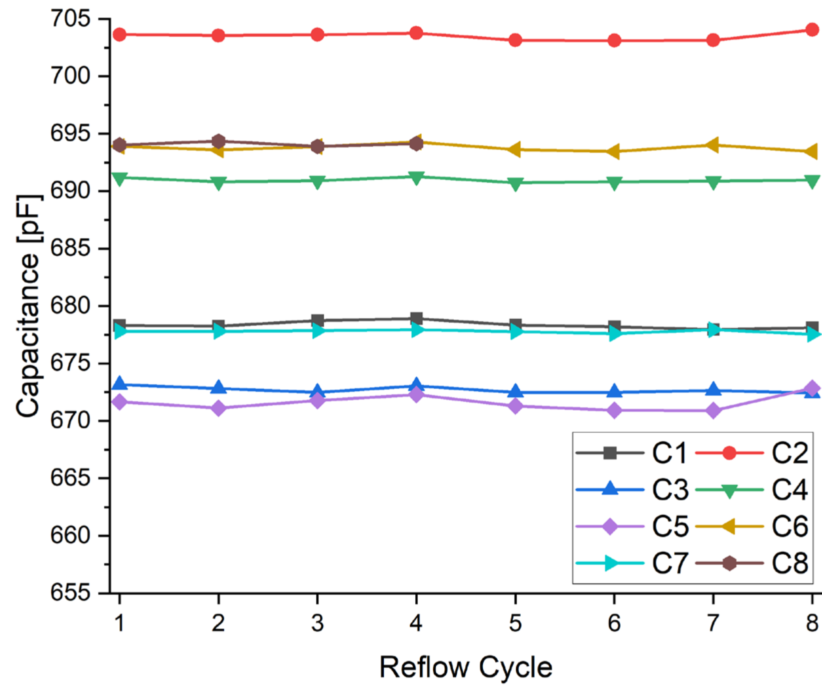

Figure 19. Cycle-Capacitance diagram of the measured values of Yageo CC1206JRNPO9BN681 (dielectric NP0, size 1206, nominal capacitance 680 pF ± 5%) for eight reflow cycles. The values remain mainly constant, with very small deviations.

Table 4. Summary of the measured changes in capacitance for the different MLCCs.

Component Type	Dielectric	Relative Change after Second Reflow	Relative Change between Subsequent Reflows	Largest Averaged Change Compared to Initial Value	Averaged Change after Eight Reflows Compared to Initial Value	Estimated Uncertainty of Measured Values
KEMET C1206C106K4PAC7800+	X5R	3–5.5%	−2.5–3.5%	5.3%	5.2%	±0.5%
KEMET C1206C474K5RACTU	X7R	2.2–4.2%	−1.8–2.6%	3.8%	3.8%	±0.2%
Yageo CC1206ZPY5V7BB475	Y5V	9.5–13%	−7–10%	14.8%	12.4%	±0.5%
Yageo CC1206JRNPO9BN681	NP0	−0.2–0.2%	−0.2–0.2%	0.2%	0.2%	±0.2%

3.3. Shear Tests

The results of the shear tests conducted with a cross-head speed of 0.1 mm/s are shown in Figure 20. The fracture force values were transferred to their corresponding shear strengths using the following equation:

$$\tau = F/A, \quad (1)$$

where τ is the shear strength, F is the force, and A = 1.85 mm^2 is the sum of the areas of both soldering pads (corresponding to the contact area).

Starting with a mean shear strength of 45.71 MPa, there are only slight variations during the following reflow cycles, with a minimum of 44.51 MPa after four cycles and a final value of 45.14 MPa. Even if no statistics can be derived from the experiments due to

the small number of samples, the shear strength of the solder joints does not really appear to change with the number of reflow cycles.

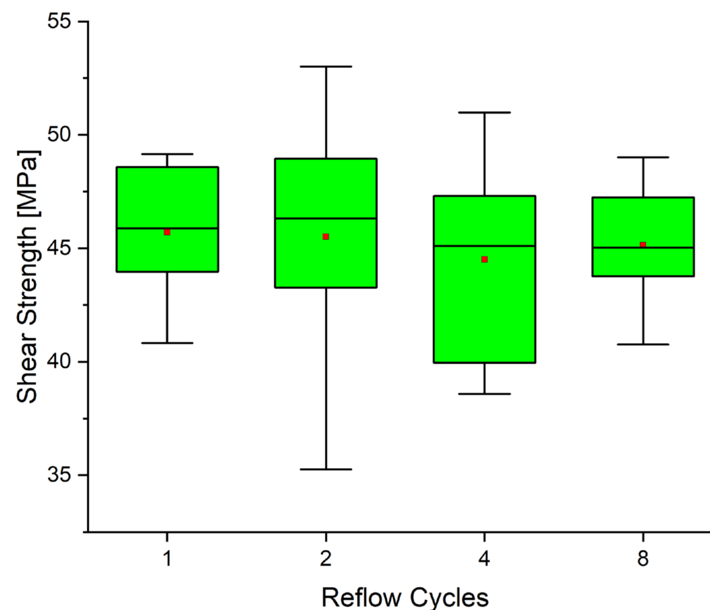

Figure 20. Results of the shear test with respect to the number of reflow cycles conducted The green box marks the first and third quartiles, the black line within the box marks the median, and the red dot marks the mean.

The tested samples were metallographically prepared to analyze the fracture path with EDX. Figures 21–24 show the results of these analyses. Each figure contains a SEM-photograph that shows the entire fracture through the solder joint and one more detailed SEM photograph that shows only the residuals of the fractured solder joint in the gap region. Corresponding EDX-mappings are depicted for both SEM photographs.

Figure 21 shows the fracture path of the shear test after one reflow cycle. It can be seen that across the entire gap region, the crack path runs along the interface to the Al_2O_3 ceramic body of the chip resistor. At the corner where the gap region ends, the crack continues its path through the meniscus of the solder joint. It can be recognized from the EDX mappings in Figure 21c,d that the Ni-thick film layer has neither adhered to the Al_2O_3 ceramic body nor to the solder. Figure 21c reveals that some residues of an Ag-metallization can still be found on the Al_2O_3 body surface.

The course of the crack path found for the shear tests after two, four, and eight reflow cycles (Figures 22–24) is very similar to that after one reflow cycle. However, in contrast to the EDX-mapping in Figure 21d, the EDX-mappings in Figures 22d, 23d and 24d show that the Ni-thick film layer adheres to the solder joint across the gap region. Moreover, the mappings show that the Ag-metallization and parts of the Al_2O_3 body can be found on top of that Ni-layer in the gap region, while the mappings depicted in Figures 22c and 24c reveal that only Al_2O_3 can be found on the opposite fracture surface, the component side. This indicates that the formation of the Cu_6Sn_5 IMC on top of the Ni thick film metallization, which occurs from the second reflow on (see Figures 11–13), increases the cohesion between solder and component metallization to a value that is higher than that for the cohesion of thick film metallization on the Al_2O_3 ceramic body of the component. Thus, the latter seems to determine the shear strength, since it is reasonable to assume that the fracture force will not increase when the crack runs through the softer solder material of the meniscus.

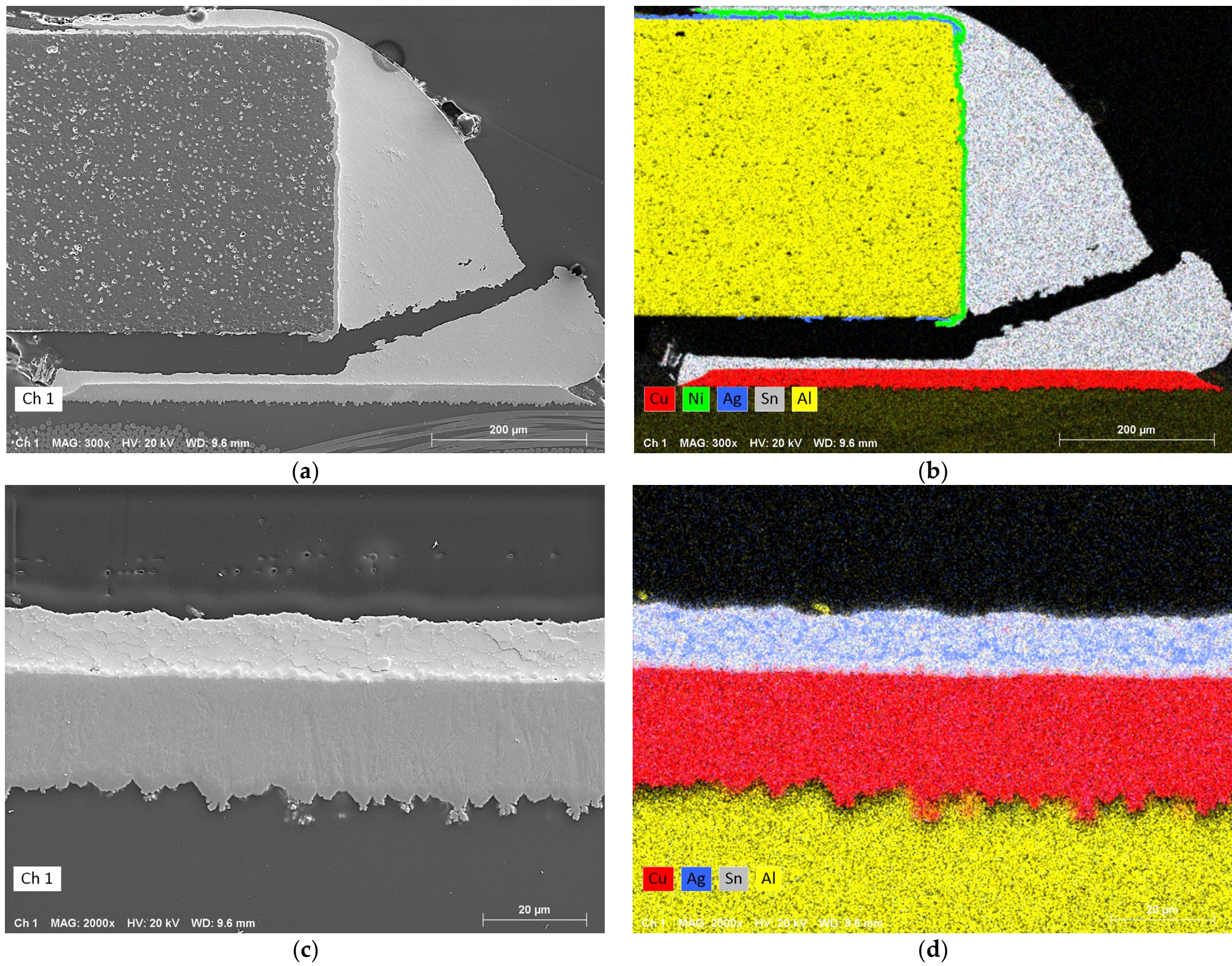

(**a**) (**b**) (**c**) (**d**)

Figure 21. EDX analysis of a shear tested resistor after one reflow cycle. (**a**) SEM image in SE mode with a magnification of 300× and (**b**) associated combined EDX map of Cu, Ni, Ag, Sn and Al. (**c**) Detailed SEM image in SE mode of the location between the ragged resistor and the Cu pad of the PCB with a higher magnification of 2000× and (**d**) associated combined EDX map of Cu, Ag, Sn, and Al (here, the Ni barrier neither adhered to the ceramic body nor to the solder). For each pair of pictures, the same settings were used.

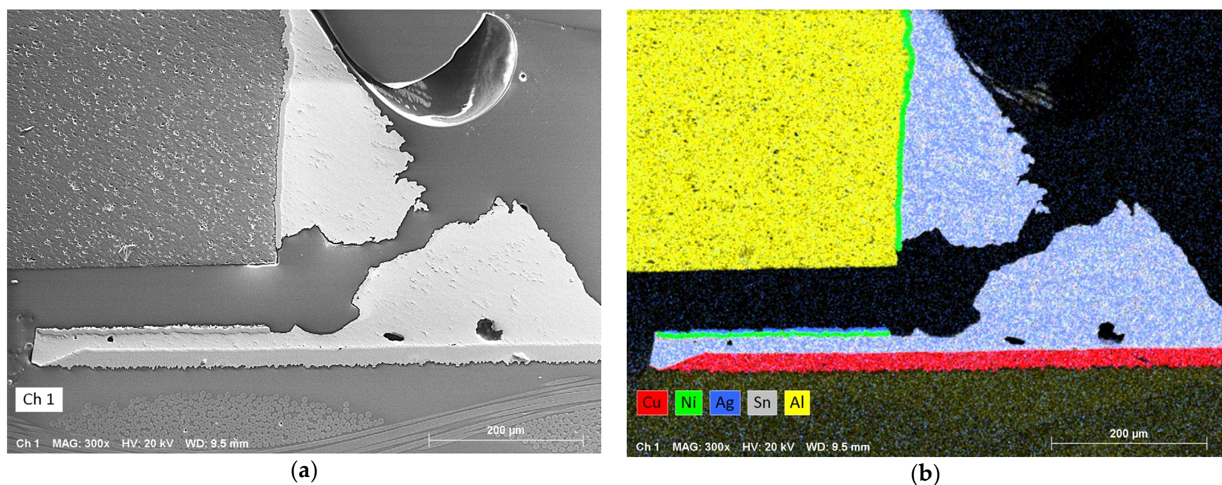

(**a**) (**b**)

Figure 22. *Cont.*

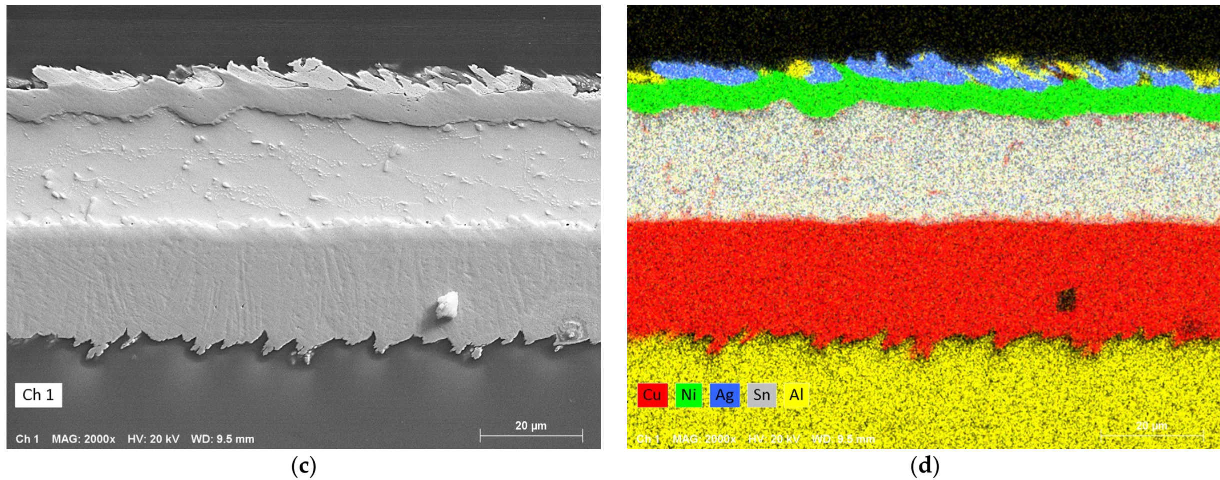

(**c**) (**d**)

Figure 22. EDX analysis of a shear tested resistor after two reflow cycles. (**a**) SEM image in SE mode with a magnification of 300× and (**b**) associated combined EDX map of Cu, Ni, Ag, Sn and Al. (**c**) Detailed SEM image in SE mode of the location between the ragged resistor and the Cu pad of the PCB with a higher magnification of 2000× and (**d**) associated combined EDX map of Cu, Ni, Ag, Sn, and Al. For each pair of pictures, the same settings were used.

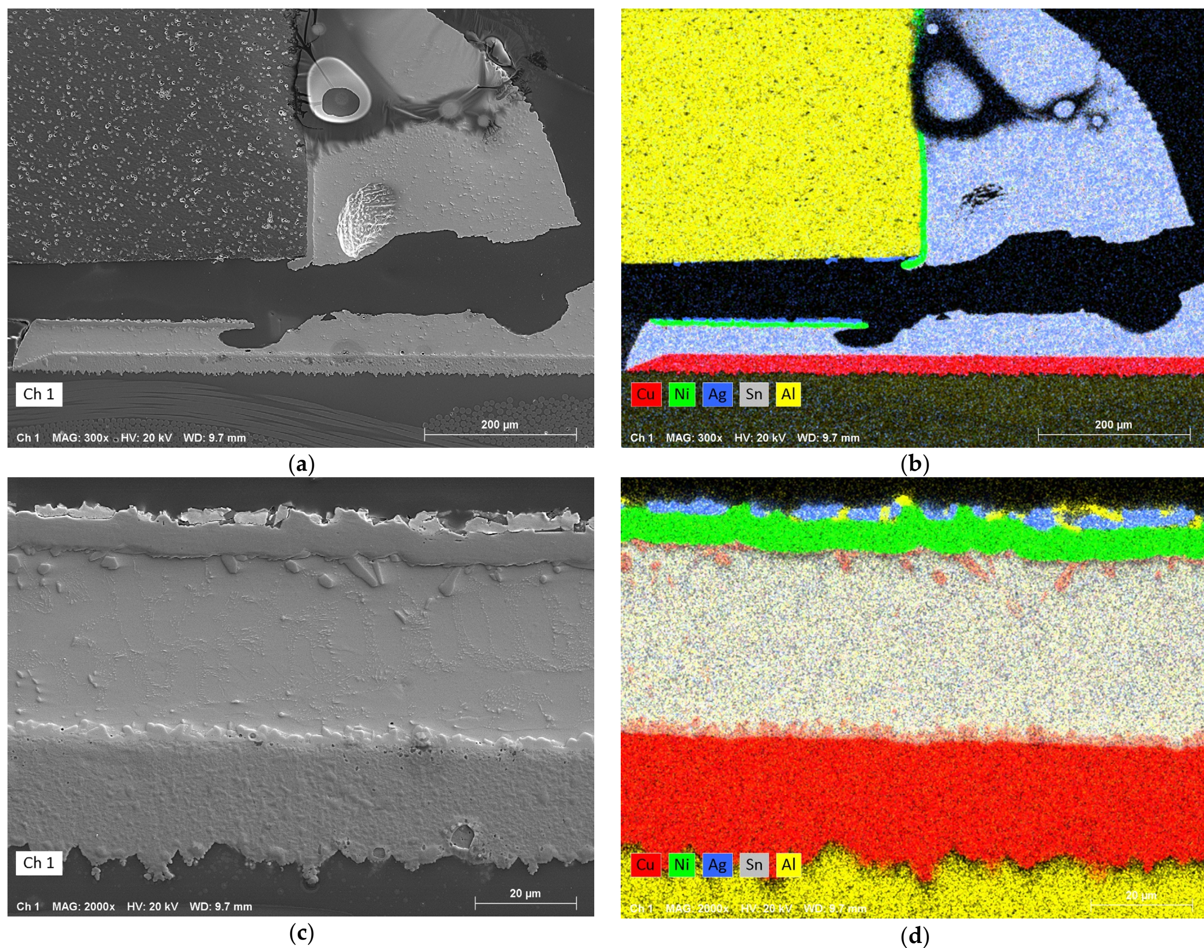

(**a**) (**b**)

(**c**) (**d**)

Figure 23. EDX analysis of a shear tested resistor after four reflow cycles. (**a**) SEM image in SE mode with a magnification of 300× and (**b**) associated combined EDX map of Cu, Ni, Ag, Sn and Al. (**c**) Detailed SEM image in SE mode of the location between the ragged resistor and the Cu pad of the PCB with a higher magnification of 2000× and (**d**) associated combined EDX map of Cu, Ni, Ag, Sn, and Al. For each pair of pictures, the same settings were used.

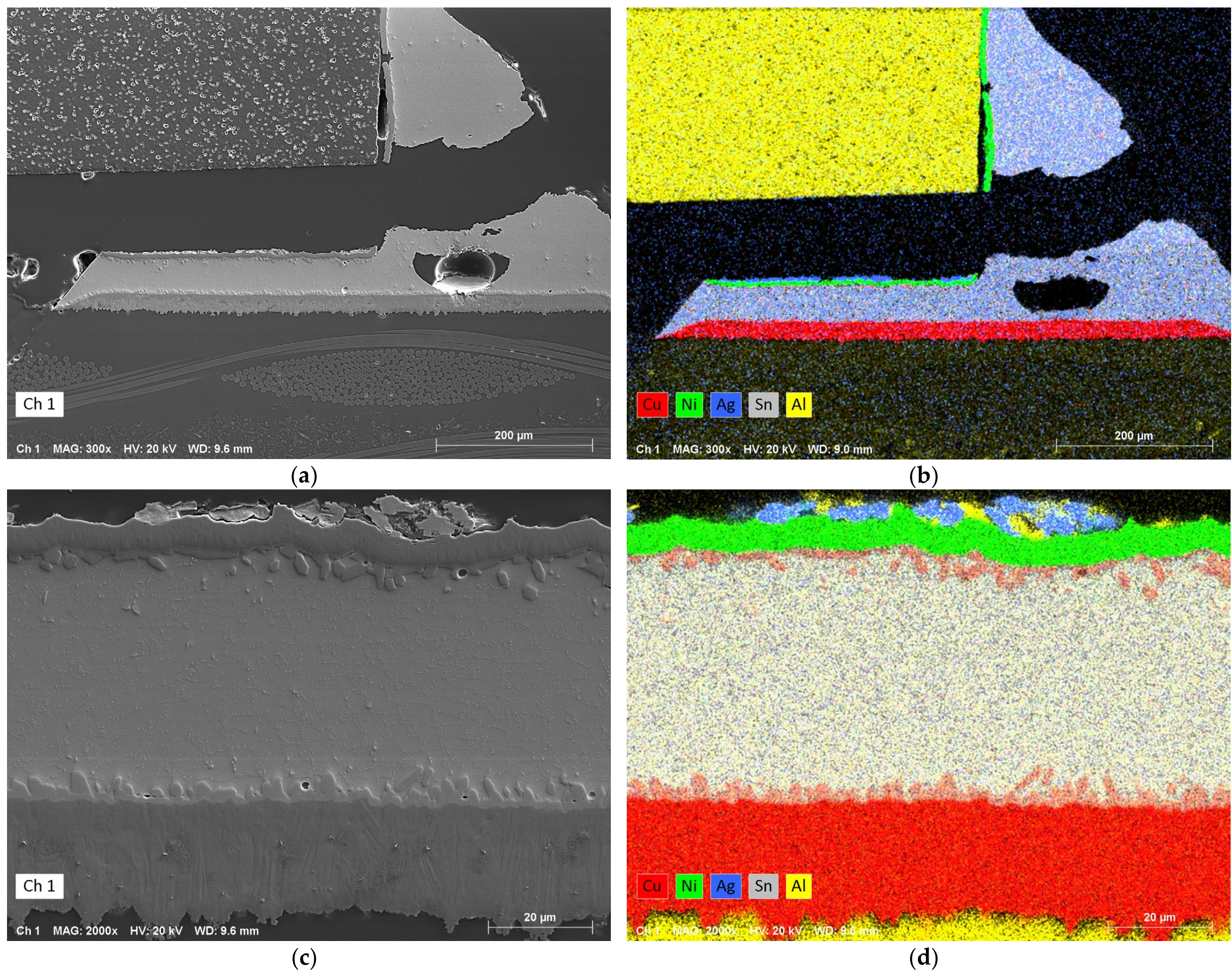

Figure 24. EDX analysis of a shear tested resistor after eight reflow cycles. (**a**) SEM image in SE mode with a magnification of 300× and (**b**) associated combined EDX map of Cu, Ni, Ag, Sn and Al. (**c**) Detailed SEM image in SE mode of the location between the ragged resistor and the Cu pad of the PCB with a higher magnification of 2000× and (**d**) associated combined EDX map of Cu, Ni, Ag, Sn, and Al. For each pair of pictures, the same settings were used.

This assumption is supported by the light microcopy pictures shown in Figure 25. The four pictures show the strength of the two component solder joints after one reflow (Figure 25a), after two reflows (Figure 25b), after four reflows (Figure 25c), and after eight reflows (Figure 25d). While the solder meniscus is uncracked, a crack path between the Al_2O_3 ceramic body and the solder joint across the gap region can be observed in all four cases. It needs to be noted that the effect of a stronger and weaker joint was only observed for roughly 50% of the shear test. The other 50% showed a full crack through both solder joints of the chip resistor.

The EDX mapping in Figures 21d, 22d, 23d and 24d indicates that the results from the shear tests on chip resistors can be transferred to the case of MLCCs. Although the metallization system is slightly different (Ag-Ni for chip resistors and Cu-Ni for MLCCs), the formation of the Cu_6Sn_5 IMC on the Ni-thick film/solder interface seems to be similar for both components. Thus, a comparable cohesion between the component metallization and the solder joint should be expected for the MLCCs.

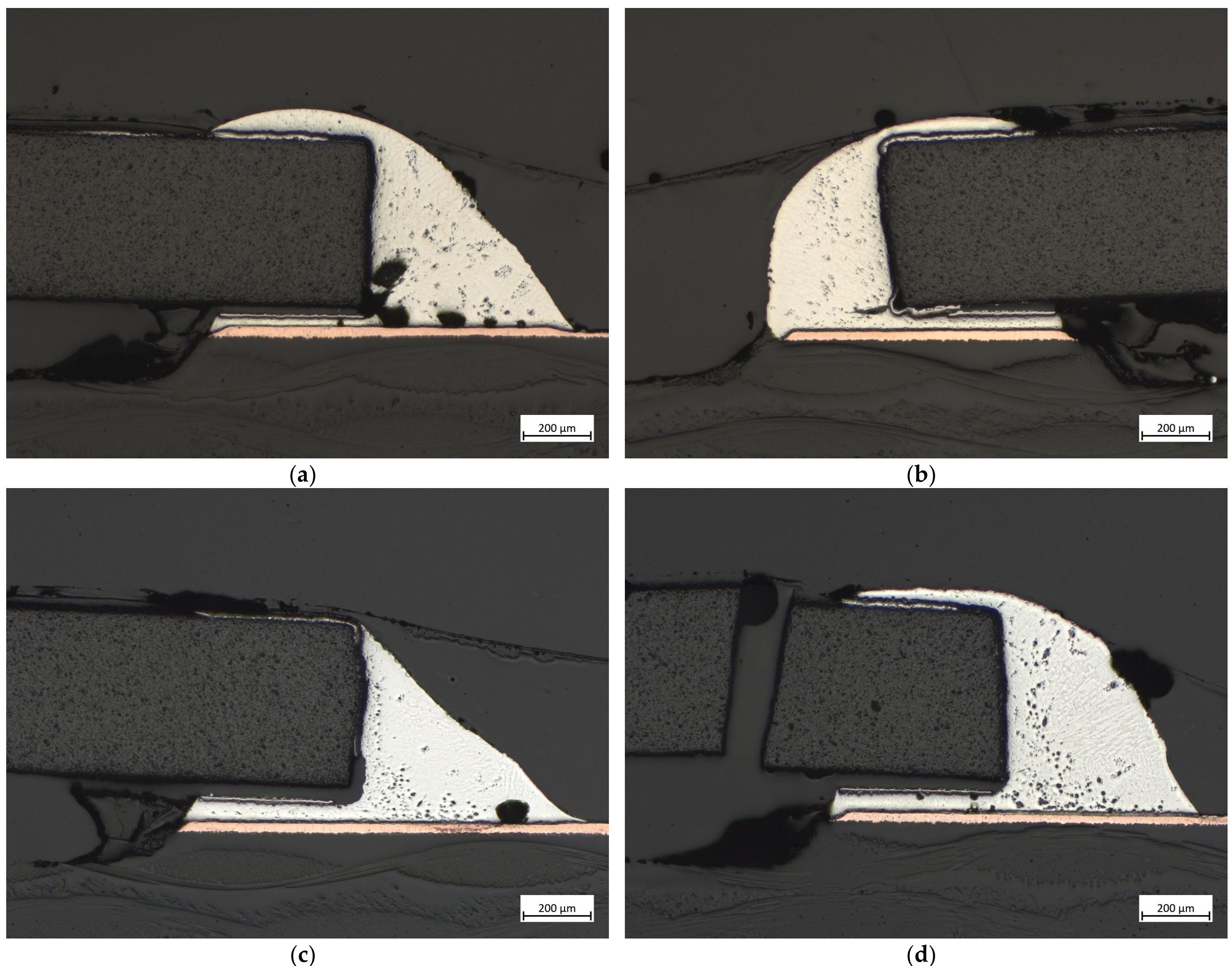

(a) (b) (c) (d)

Figure 25. Light microscopy images with a magnification of 5× of the non-ragged side of resistors after the shear test after (**a**) one, (**b**) two, (**c**) four, and (**d**) eight reflow cycles.

4. Discussion

During a reflow cycle, the formation of a proper Cu_6Sn_5 IMC within the solder paste is necessary to achieve a strong and reliable bond between the component and the Cu metallization of a PCB. However, due to the much higher brittleness of the IMC compared to the individual materials, the thickness of this formation should be kept to a minimum. In times of significantly increased demand for a reduction in environmental pollution, the reuse of components gets more and more important. In this framework, some components will have to experience multiple reflow cycles, resulting in a small but constant increase in the IMC layer thickness, as the experiments show.

Although this average IMC layer thickness grows in a similar way on both the PCB side and component side, the morphology differs. While there seems to be linear growth on the PCB side with nearly no variability (coefficient of determination, R^2 = 0.96), a lot of variability compared to the linear growth can be observed on the component side (R^2 = 0.54). This variability is supposedly caused by the inhomogeneous, rather dendritic, growth of Cu_6Sn_5 IMC on the component side compared to the equally distributed spherical growth kinetics of the Cu_6Sn_5 IMC on the PCB side. The Cu_6Sn_5 IMC on the component side, which requires the transport of Cu from the PCB-Side trough the solder joint, might be responsible for the decomposition of the solder material, which shows in a depletion of

the silver in towards the Cu_6Sn_5 IMCs. This effect is particularly pronounced after the first and second reflows, when the Cu_6Sn_5 IMCs start to form and grow. However, in order to precisely describe and understand the formation of the Cu_6Sn_5 IMC on the Ni-thick film layer and the depletion of Ag towards Cu_6Sn_5 IMC, similar experiments to those reported [19] have to be carried out.

Depending on the number of reflow cycles, the capacitance of most of the usual types of MLCC changes. After the first reflow cycle, all the measured capacitance values are still in the ranges that were specified by the respective manufacturer. Some of the samples were out of range after two (X7R) or three (Y5V) reflow cycles or increased almost to the upper limit (Y5V) after several reflow cycles. It was observed that existing differences between the MLCC samples do not change and remain. While the highest change in capacitance with 12.4% could be observed for Y5V MLCCs (class III), the change was in mid-range with 3.8% to 5.3% for X5R and X7R MLCCs (class II) and 0.2% for NP0 MLCCs (class I). The reason for the different changes in capacitance is the use of different materials as dielectrics. The X5R and X7R bodies are based on ferroelectric $BaTiO_3$ and different dopants ($\varepsilon_r = 10^3 \ldots 10^4$), which exhibit high polarizability, which in turn depends on mechanical stress, among other things. The heat input that is caused by the multiple reflow cycles evokes thermomechanical stress within the MLCC component due to the different coefficients of thermal expansion of the component, the PCB, and the solder paste. This thermomechanical stress remains as residual stress within the component, affecting the polarizability and thus the permittivity, resulting in a change in capacitance. The Y5V bodies are also based on ferroelectric $BaTiO_3$, but with other dopants to increase the polarizability and thus the permittivity and capacitance, respectively, which is why the changes are relatively the highest. In contrast, the NP0 bodies consist of a paraelectric dielectric (e.g., $CaZrO_3$), which offers a much lower permittivity ($\varepsilon_r << 10^2$) and thus much lower capacitance values, which cannot be polarized, and the capacitance remains almost constant during the experiments. The measured values are in accordance with the observations made in [25].

Up to now, it appears that the described changes in the microstructure of the solder (e.g., the change in the Ag distribution within the solder) and in the thickness of the IMC layers (from 2 μm up to 5 μm) do not seriously affect the mechanical stability of the solder joints: the measured mean shear strengths vary in the range from 44.51 MPa to 45.71 MPa (corresponding to a relative change of less than 3%) for the different reflow cycle numbers. The microscopical analysis of the samples reveals that the metallization is always detached from the body of the resistor after a crack was detected during the experiment. In the moment of the detachment, the solder paste is carried away by the breaking metallization. It can be assumed that the cohesion of the metallization/component interface is lower than the cohesion on the metallization/solder interface because the crack would otherwise run differently, most probably up to the inner end of the Cu pad. This weakness of the metallization might be a reason for the very small change in the measured shear strengths. In contrast, other publications report larger changes of approximately 10% to 20% at similar IMC layer thicknesses [15,21,23,24], or similar changes of approximately 5% at slightly higher IMC layer thicknesses of 3 μm to 8.5 μm [16]. Another important effect that could not be observed here might be the problem of detaching Cu metallization after several reflow cycles, as reported in [21].

5. Conclusions

In the context of reusing electronic components, it is necessary to have an accurate knowledge of the effects of multiple reflow cycles on the formation of IMCs and the decomposition of the solder paste used. Therefore, up to eight reflow cycles were performed on various kinds of MLCCs of size 1206 with different capacitance values and dielectric types (X5R, X7R, Y5V, and NP0). Electrical four-point capacitance measurements were performed after each cycle, showing an average increase after eight cycles of 5.2% (X5R), 3.8% (X7R), and 12.4% (Y5V), while almost no change in capacitance could be observed

in the case of the NP0 MLCCs. Depending on the tolerance of the selected components, a change in capacitance due to the reuse of MLCCs may be another factor that needs to be considered during the circuit design.

After one, two, four, and eight reflow cycles, cross sections of the samples were made, and both SEM and EDX analyses were performed to investigate the changes at the Cu/solder and the component/solder interfaces. While a proper Cu_6Sn_5 IMC layer is already formed at the interface solder/PCB metallization after the first reflow cycle, there are only small individual Cu_6Sn_5 cells formed at the interface solder/component metallization. These small cells experience significant growth during the second reflow cycle, although they still do not form a coherent layer. Further reflow cycles result in a similar increase in both IMC thicknesses. At the same time, an Ag depletion zone could be found at the interface solder/PCB metallization after the first reflow cycle, resulting in a second Ag depletion zone at the interface solder/component metallization after the second reflow cycle. During the following reflow cycles, the Ag is distributed more and more within the solder and Ag-depleted zones diminish, while the pure beta-tin areas and the Ag_3Sn/Sn layers continuously shrink.

To investigate the influence of these changes on the solder joint mechanical functionality, shear tests were conducted on small PCBs with resistors of size 1206 after different numbers of reflow cycles. During the experiments, the resistance was measured continuously to detect a crack within the solder joints as soon as possible. With a minimum mean shear strength of 44.51 MPa after four cycles and a maximum shear strength of 45.71 MPa after one cycle, multiple reflow cycles do not appear to have any significant influence on mechanical robustness.

Author Contributions: Conceptualization, E.W. and S.W.; methodology, E.W. and S.W.; investigation, E.W.; writing, E.W. and S.W.; review and editing, E.W. and S.W.; supervision, S.W. All authors have read and agreed to the published version of the manuscript.

Funding: This research received no external funding.

Data Availability Statement: The original contributions presented in the study are included in the article, further inquiries can be directed to the corresponding author.

Acknowledgments: The authors would like to offer particular thanks to G. S. Dekate for assistance in electrical measurements, to D. Barth for his help in sample preparation and mechanical characterization, and to A. Ruh for his support in SEM/EDX analysis and in editing graphics.

Conflicts of Interest: The authors declare no conflicts of interest.

References

1. Goosey, M.; Kellner, R. Recycling technologies for the treatment of end of life printed circuit boards (PCBs). *Circuit World* **2003**, *29*, 33–37. [CrossRef]
2. Chancerel, P.; Meskers, C.E.M.; Hagelüken, C.; Rotter, V.S. Assessment of Precious Metal Flows During Preprocessing of Waste Electrical and Electronic Equipment. *J. Ind. Ecol.* **2009**, *13*, 791–810. [CrossRef]
3. Ramon, H.; Peeters, J.R.; Sterkens, W.; Duflou, J.R.; Kellens, K.; Dewulf, W. Techno-economic potential of recycling Tantalum containing capacitors by automated selective dismantling. *Procedia CIRP* **2020**, *90*, 421–425. [CrossRef]
4. Maurice, A.A.; Dinh, K.N.; Charpentier, N.M.; Brambilla, A.; Gabriel, J.-C.P. Dismantling of Printed Circuit Boards Enabling Electronic Components Sorting and Their Subsequent Treatment Open Improved Elemental Sustainability Opportunities. *Sustainability* **2021**, *13*, 10357. [CrossRef]
5. Wang, J.; Guo, J.; Xu, Z. An environmentally friendly technology of disassembling electronic components from waste printed circuit boards. *Waste Manag.* **2016**, *53*, 218–224. [CrossRef]
6. Jiang, P.; Harney, M.; Song, Y.; Chen, B.; Chen, Q.; Chen, T.; Lazarus, G.; Dubois, L.H.; Korzenski, M.B. Improving the end-of-Life for electronic materials via sustainable recycling methods. *Procedia Environ. Sci.* **2012**, *16*, 485–490. [CrossRef]
7. Conti, M.; Orcioni, S. Modeling of Failure Probability for Reliability and Component Reuse of Electric and Electronic Equipment. *Energies* **2020**, *13*, 2843. [CrossRef]
8. Kopacek, B. Intelligent disassembly of components from printed circuit boards to enable re-use and more efficient recovery of critical metals. In Proceedings of the 2016 Electronics Goes Green 2016+(EGG), Berlin, Germany, 6–9 September 2016; pp. 190–195.

9. Stobbe, I.; Potter, H.; Griese, H.; Fotheringham, G.; Reichl, H. Quality Challenges of Reused Components. In Proceedings of the 2004 International IEEE Conference on the Asian Green Electronics (AGEC), Hong Kong, Shenzhen, China, 7–9 January 2004; pp. 218–225.
10. Yuile, A.; Wiss, E.; Barth, D.; Wiese, S. Simulation of Mechanical Stresses in $BaTiO_3$ Multilayer Ceramic Capacitors during Desoldering in the Rework of Electronic Assemblies Using a Framework of Computational Fluid Dynamics and Thermomechanical Models. *Materials* **2024**, *17*, 2702. [CrossRef]
11. Xiang, D.; Pang, Z.; Long, D.; Mou, P.; Yang, J.; Duan, G. The Disassembly Process and Apparatus of waste Printed Circuit Board Assembly for reusing the components. *Appl. Mech. Mater.* **2014**, *457*, 474–485. [CrossRef]
12. Koo, J.M.; Lee, Y.H.; Kim, S.K.; Jeong, M.Y.; Jung, S.B. Mechanical and Electrical Properties of Sn-3.5 Ag Solder/Cu BGA Packages during Multiple Reflows. *Key Eng. Mater.* **2005**, *297*, 801–806. [CrossRef]
13. Koo, J.M.; Lee, C.Y.; Jung, S.B. Effect of Reflow Number on Mechanical and Electrical Properties of Ball Grid Array (BGA) Solder Joints. *J. Microelectron. Packag. Soc.* **2007**, *14*, 71–77.
14. Kim, D.G.; Kim, J.W.; Ha, S.S.; Noh, B.I.; Koo, J.M.; Park, D.W.; Ko, M.W.; Jung, S.B. Effect of reflow numbers on the interfacial reaction and shear strength of flip chip solder joints. *J. Alloys Compd.* **2008**, *458*, 253–260. [CrossRef]
15. Noh, B.I.; Koo, J.M.; Kim, J.W.; Kim, D.G.; Nam, J.D.; Joo, J.; Jung, S.B. Effects of number of reflows on the mechanical and electrical properties of BGA package. *Intermetallics* **2006**, *14*, 1375–1378. [CrossRef]
16. Zhong, W.H.; Chan, Y.C.; Alam, M.O.; Wu, B.Y.; Guan, J.F. Effect of multiple reflow processes on the reliability of ball grid array (BGA) solder joints. *J. Alloys Compd.* **2006**, *414*, 123–130. [CrossRef]
17. Salleh, M.M.; McDonald, S.D.; Gourlay, C.M.; Yasuda, H.; Nogita, K. Suppression of Cu_6Sn_5 in TiO_2 reinforced solder joints after multiple reflow cycles. *Mat. Des.* **2016**, *108*, 418–428.
18. Ma, H.R.; Wang, Y.P.; Chen, J.; Ma, H.T.; Zhao, N. The effect of reflow temperature on IMC growth in Sn/Cu and Sn0.7Cu/Cu solder bumps during multiple reflows. In Proceedings of the 18th International Conference on Electronic Packaging Technology (ICEPT), Harbin, China, 16–19 August 2017; pp. 1402–1405.
19. Ma, H.; Ma, H.; Kunwar, A.; Shang, S.; Wang, Y.; Chen, J.; Huang, M.; Zhao, N. Effect of initial Cu concentration on the IMC size and grain aspect ratio in Sn-xCu solders during multiple reflows. *J. Mater. Sci. Mater. Eletron.* **2018**, *29*, 602–613. [CrossRef]
20. Huang, R.; Ma, H.; Shang, S.; Kunwar, A.; Wang, Y.; Ma, H. Size effect on interface reaction of Sn–x Cu/Cu solder joints during multiple reflows. *J. Mater. Sci. Mater. Electron.* **2019**, *30*, 4359–4369. [CrossRef]
21. Liu, P.; Yao, P.; Liu, J. Effects of multiple reflows on interfacial reaction and shear strength of SnAgCu and SnPb solder joints with different PCB surface finishes. *J. Alloys Compd.* **2009**, *470*, 188–194. [CrossRef]
22. Gao, H.; Wei, F.; Sui, Y.; Qi, J. Growth behaviors of intermetallic compounds on the Sn-0.7Cu-10Bi-*x*Co/Co interface during multiple reflow. *Mater. Des.* **2019**, *174*, 107794. [CrossRef]
23. Branzei, M.; Plotog, I.; Miculescu, F.; Varzaru, G.; Svasta, P.; Thumm, A. Solder Joints Properties as Function of Multiple Reflow Vapor Phase Soldering Process. In Proceedings of the 35th International Spring Seminar on Electronics Technology (ISSE), Bad Aussee, Austria, 9–13 May 2012; pp. 155–160.
24. Wirth, V.; Rendl, K.; Steiner, F. Effect of Multiple Reflow Cycles on Intermetallic Compound Creation. In Proceedings of the 38th International Spring Seminar on Electronics Technology (ISSE), Eger, Hungary, 6–10 May 2015; pp. 226–230.
25. Jánó, R.; Fodor, A. Soldering Profile Optimization for Through-Hole and Surface Mounted Ceramic Capacitors. In Proceedings of the 37th International Spring Seminar on Electronics Technology (ISSE), Dresden, Germany, 7–11 May 2014; pp. 170–175.
26. Jánó, R.; Pitică, D.; Svasta, P.; Vărzaru, G. Effects of Reflow Soldering Methods on the Lifetime of Capacitors. In Proceedings of the 35th International Spring Seminar on Electronics Technology (ISSE), Bad Aussee, Austria, 9–13 May 2012; pp. 183–188.
27. Kim, M.-G.; Lee, B.H.; Yun, T.-Y. Equivalent-Circuit Model for High-Capacitance MLCC Based on Transmission-Line Theory. *IEEE Trans. Compon. Packag. Manuf. Technol.* **2011**, *2*, 1012–1020. [CrossRef]
28. *IEC 60384-1*; Fixed Capacitors for Use in Electronic Equipment—Part 1: Generic Specification. International Electrotechnical Commission: Geneva, Switzerland, 2021.
29. Wiss, E.; Barth, D.; Wiese, S. Concept of a Mechanical Test Setup for Packaging Materials Using Digital Image Correlation Methods. In Proceedings of the 22nd International Conference on Thermal, Mechanical and Multi-Physics Simulation and Experiments in Microelectronics and Microsystems (EuroSimE), Online, 19–21 April 2021; pp. 1–6.
30. Anthati, S.G.; Wiss, E.; Wiese, S. Bending Experiments on QFN Components. In Proceedings of the 25th International Conference on Thermal, Mechanical and Multi-Physics Simulation and Experiments in Microelectronics and Microsystems (EuroSimE), Catania, Italy, 7–10 April 2024; pp. 1–5.
31. *IEC 62137-1-2*; Surface Mounting Technology—Environmental and Endurance Test Methods for Surface Mount Solder Joint—Part 1–2: Shear Strength Test. International Electrotechnical Commission: Geneva, Switzerland, 2007.
32. Amli, S.F.M.; Salleh, M.A.A.M.; Aziz, M.S.A.; Yasuda, H.; Nogita, K.; Abdullah, M.M.A.B.; Nemes, O.; Sandu, A.V.; Vizureanu, P. Effects of Multiple Reflow on the Formation of Primary Crystals in Sn-3.5Ag and Solder Joint Strength: Experimental and Finite Element Analysis. *Materials* **2023**, *16*, 4360. [CrossRef] [PubMed]

Disclaimer/Publisher's Note: The statements, opinions and data contained in all publications are solely those of the individual author(s) and contributor(s) and not of MDPI and/or the editor(s). MDPI and/or the editor(s) disclaim responsibility for any injury to people or property resulting from any ideas, methods, instructions or products referred to in the content.